

# From underground natural gas to hydrogen storage in fractured reservoir rock : comparing relative permeabilities for hydrogen versus methane and nitrogen

Sojwal Manoorkar<sup>a,b,\*</sup>, Gülce Kalyoncu Pakkaner<sup>a,b</sup>, Hamdi Omar<sup>a,b</sup>, Soetkin Barbaix<sup>a,b</sup>, Dominique Ceursters<sup>c</sup>, Maxime Lathinis<sup>c</sup>, Stefanie Van Offenwert<sup>c</sup>, Tom Bultreys<sup>a,b</sup>

<sup>a</sup>*Department of Geology, Ghent University, Ghent, Belgium*

<sup>b</sup>*Centre for X-ray Tomography (UGCT), Ghent University, Ghent, Belgium*

<sup>c</sup>*Fluxys, Belgium*

---

## Abstract

Underground hydrogen storage in saline aquifers is a potential solution for seasonal renewable energy storage. Among potential storage sites, facilities used for underground natural gas storage have advantages, including well-characterized cyclical injection-withdrawal behavior and partially reusable infrastructure. However, the differences between hydrogen-brine and natural gas-brine flow, particularly through fractures in the reservoir and the sealing caprock, remain unclear due to the complexity of two-phase flow. Therefore, we investigate fracture relative permeability for hydrogen versus methane (natural gas) and nitrogen (commonly used in laboratories). Steady-state relative permeability experiments were conducted at 10 MPa on fractured carbonate rock from the Loenhout natural gas storage in Belgium, where

---

\*I am corresponding author

*Email address:* sojwal.manoorkar@UGent.be/sojwal.m@gmail.com (Sojwal Manoorkar )

gas flows through  $\mu\text{m}$ -to- $\text{mm}$  scale fractures. Our results reveal that the hydrogen exhibits similar relative permeability curves to methane, but both are significantly lower than those measured for nitrogen. This implies that nitrogen cannot reliably serve as a proxy for hydrogen at typical reservoir pressures. The low relative permeabilities for hydrogen and methane indicate strong fluid phase interference, which traditional relative permeability models fail to capture. This is supported by our observation of periodic pressure fluctuations associated with intermittent fluid connectivity for hydrogen and methane. In conclusion, our findings suggest that the fundamental flow properties of fractured rocks are complex but relatively similar for hydrogen and natural gas. This is an important insight for predictive modeling of the conversion of Loenhout and similar natural gas storage facilities, which is crucial to evaluate their hydrogen storage efficiency and integrity.

*Keywords:* Underground hydrogen storage, Relative permeability, Fractured rock, Hydrogen, Methane

---

## 1. Introduction

The hydrogen economy is expected to play a critical role in the global transition to cleaner energy and achieving net-zero carbon emissions. A key technology supporting large-scale energy storage is Underground Hydrogen Storage (UHS). UHS enables the storage of TWh-scale energy by injecting hydrogen into depleted gas reservoirs, saline aquifers, and existing gas storage facilities. The stored (green) hydrogen can be produced by electrolysis during periods of surplus electricity generation [1, 2, 3, 4, 5, 6]. As renewable energy sources like wind and solar continue to expand [7], UHS provides a potential

solution to balance renewable energy supply and demand, enhancing energy security, and helping to decarbonize energy systems.

Converting pre-existing natural gas storage sites to hydrogen storage potentially offers advantages to using depleted gas fields or saline aquifers that have not been previously deployed for storage purposes. This includes leveraging expensive site characterization campaigns, tried-and-tested reservoir and caprock behaviour under cyclical injection-retraction operations, and existing connections to gas treatment and pipeline infrastructure. Among operational and planned natural gas storage sites in Europe, 86% are depleted gas fields and 14% are aquifers, together capable of providing up to 750 TWh of hydrogen storage [8]. Conversion of these storage resources would be sufficient for a mid-range scenario of 2,500 TWh of annual hydrogen demand by 2050, at a 30% storage capacity. In this paper, we focus on a notable example of such a natural gas storage site under investigation for hydrogen conversion: the Loenhout natural gas storage facility in northern Belgium. Loenhout is uniquely well-connected in Western Europe as it is part of a pipeline network linking Belgium, France, The Netherlands, Germany, Luxemburg and the United Kingdom, including international shipping terminals in the North Sea ports of Zeebrugge and Dunkirk. If converted successfully, it would provide 2.2 TWh of storage capacity. The site comprises a partially karstified limestone aquifer from Visean age, characterized by a fracture-dominated flow system with low primary porosity [9, 10, 11]. Its conversion is currently under investigation in the BE-Hystore project funded by the Belgian federal Energy Transition Fund and the site operator Fluxys Belgium.

Repurposing an aquifer natural gas storage site for large-scale hydrogen injection requires evaluating whether the flow of the stored gas in the pores or fractures of the storage reservoir would be affected, as this may impact injectivity and operational efficiency [12, 13]. While significant progress has been made in understanding hydrogen flow in porous media, substantial knowledge gaps remain regarding its behavior in fractured rock. This is not only important for fractured storage reservoirs such as in Loenhout, but also to assess leakage through caprock if fractures are present or generated during storage [14, 15]. A primary uncertainty in the current scientific understanding lies in hydrogen's relative permeability compared to methane's. Relative permeability is a key parameter for upscaled multiphase flow modeling, which quantifies how the flow of gas is impacted by the presence of (saline) groundwater in the reservoir, and vice versa [16].

Over the last two decades, several studies have shown that the relative permeability behaviour of fractured media differs significantly from that of porous materials due to its dependence on complex fluid dynamics [17]. Nevertheless, it is currently unclear how such complexities affect fracture relative permeabilities for hydrogen compared to other gases, particularly at elevated pressures and temperatures typical for UHS. Experiments with air-water in transparent fractures have revealed strong phase interference and reduced relative permeability at intermediate saturations in rough fractures [18, 19]. Relative permeability in such systems is highly sensitive to fracture surface roughness and aperture heterogeneity, influencing the meandering or twisting of flow paths [20, 21, 22, 23, 24]. Capillary-dominated flow, especially in low viscosity-ratio fluid systems such as hydrogen-brine and methane-brine, is



characterized by fluid pathways that are intermittently connected, caused by snap-off events and Haines jumps [25]. State-of-the-art fracture relative permeability models aim to capture the greater phase interference, the absence of percolating pathways, and altered flow patterns compared to porous media [26, 27, 28, 29, 30]. The current need for understanding how the findings above translate to UHS is underscored by a lack of experimental studies on fractured rock. This is despite significant recent efforts on the corresponding behaviour of porous reservoir rocks [31, 32, 33, 34, 35, 36, 37, 38], which are difficult to translate directly to fracture systems. Comparative studies of two-phase flow behavior of relevant fractured samples under consistent reservoir conditions are thus critical to address these uncertainties.

Assessing hydrogen flow in fractured aquifers such as Loenhout is essential to evaluate its feasibility as a storage medium in comparison to methane. Therefore, our study presents the first direct measurements of drainage relative permeability for hydrogen-brine, methane-brine, and nitrogen-brine systems in fractured limestone rock at subsurface pressure conditions of 10 MPa. The investigated rock used was collected from a depth of 1400 m at the Loenhout aquifer. Methane was selected because it is a good model for the stored gas in current natural gas storage aquifers [39], and it may serve effectively as a cushion gas. Nitrogen was selected because of its common use in laboratory experiments, and because it is a potential cushion gas in new storage sites [40]. Using X-ray computed tomography (XCT), we captured pore-scale fluid distribution within fractures during steady-state drainage. The recorded pressure fluctuations are analyzed to identify frequency of flow intermittency. By comparing the relative permeability and flow behavior of

hydrogen, methane, and nitrogen, this study contributes to a deeper understanding of gas-brine interactions in fractured systems and offers critical data to improve the accuracy of field-scale UHS models.

## 2. Materials and methods

### 2.1. Rocks and fluids

A partially karstified limestone from the Viséan (Dinantian) age was drilled from well DZH24 at the underground natural gas storage facility in Loenhout, Belgium. This limestone belongs to the Carboniferous group in the Campine-Brabant Basin of northern Belgium. The rock matrix exhibits very low porosity ( $<0.01$ ) and permeability ( $<1$  mD), indicating that fluid flow predominantly occurs through its fracture network. Previous reservoir characterization has shown that joints and partially open veins contribute to the overall permeability [41]. Since naturally fractured samples were unavailable for this study, artificially fractured samples were used as the best alternative for conducting our experiments.

A cylindrical rock core, measuring 25 mm in diameter and 45 mm in length, was drilled for the experiments in this study. The core was wrapped in Teflon tape and fractured using the Brazilian tensile stress method at Ghent University's concrete lab. This technique was selected to generate a fracture network that closely mimics natural conditions, with variable fracture width and surface roughness as shown in Figure 1. The dry fracture image and the porosity distribution along the core are shown in Figure 4b, with the average measured porosity being 0.011. Flow through rough fractures is governed by variable aperture and relative roughness, characterized by the

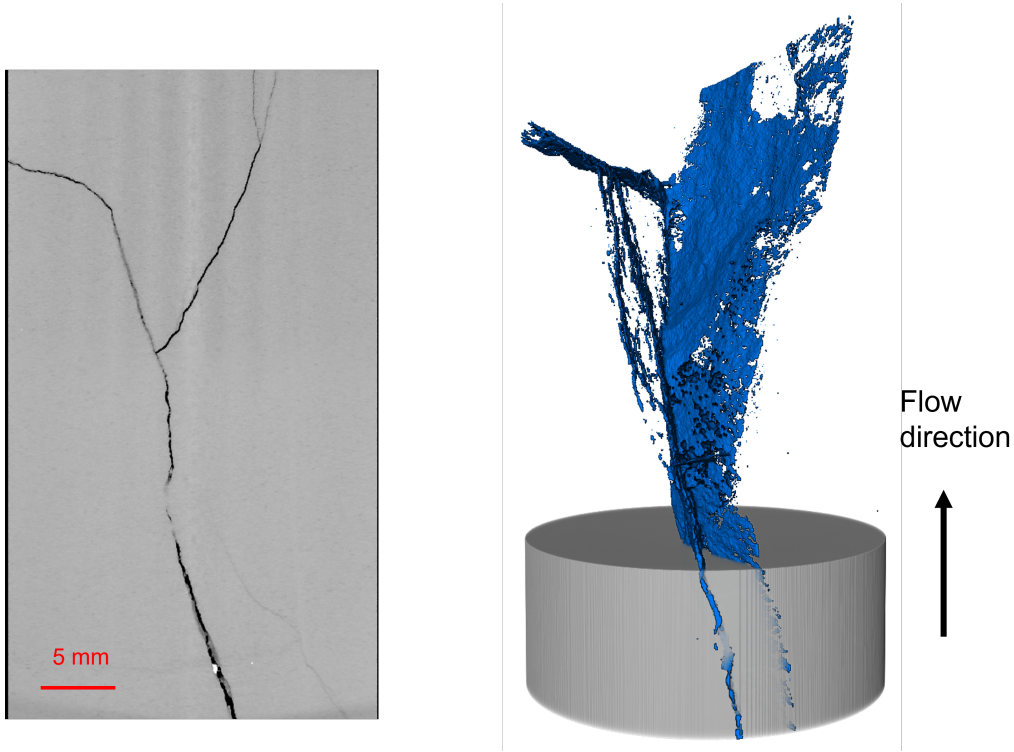


Figure 1: (left) A center slice of dry scan image of the rock core. (right) 3D rendering of fracture network of the rock core.

roughness index,  $\lambda_b = \frac{\langle b \rangle^\sigma}{\langle b \rangle}$ , where  $\langle b \rangle^\sigma$  represents the standard deviation of the aperture distribution, and  $\langle b \rangle$  is the mean aperture. Aperture was obtained from the segmented dry scan using the ‘PoreSpy’ Python toolkit [42], which calculates local thickness as shown in Figure 2a. The aperture distribution is shown in Figure 2b, with a mean aperture  $\langle b \rangle$  of 350  $\mu\text{m}$ . The relative roughness index was calculated to be 0.61.

The wetting phase was prepared by dissolving 25 wt% potassium iodide (Sigma Aldrich) in deionized water, which enhanced X-ray contrast for imaging purposes. The brine was selected to provide optimal contrast for X-ray imaging. While its composition differs from the natural reservoir brine, key

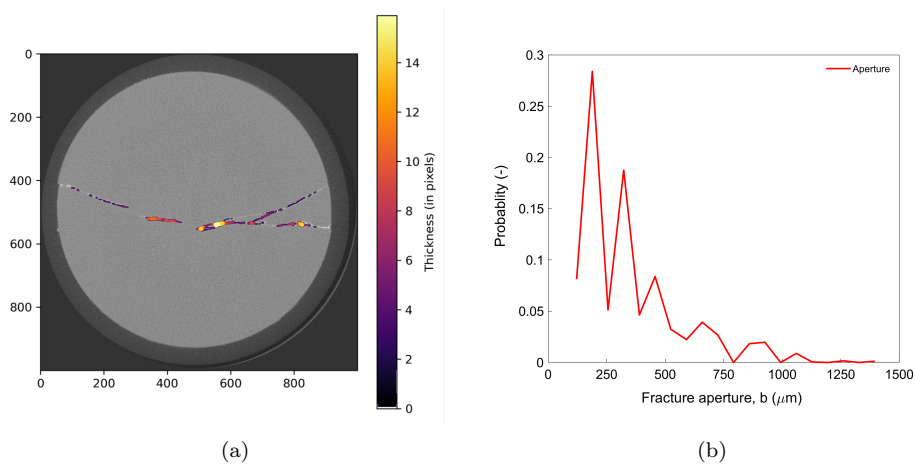


Figure 2: (a) A 2D local thickness map of a horizontal slice of dry scan. (b) Aperture (local thickness) distribution with  $\langle b \rangle = 350 \mu\text{m}$ .

properties influencing relative permeability, such as surface tension and viscosity, remain comparable and should not significantly impact the results. As non-wetting phases, high-purity ( $>99.99\%$ )  $\text{H}_2$ ,  $\text{CH}_4$  and  $\text{N}_2$  gases (supplied by Air Liquide) were used. The thermophysical properties of these gases are listed in Table 1 and parameter space used in this study are shown in Figure 4a. We maintained the same flow rate instead of matching the capillary number, as the reservoir properties are fixed. Given that nitrogen and methane are used as cushion gases, it is more practical to keep the injection rate consistent rather than focusing on the capillary number. Notably, the capillary number for all flow rates and gases is less than  $10^{-5}$ , indicating that the flow is capillary-dominated and exhibits similar flow regimes. It should be noted that the experimental temperature does not match the reservoir temperature due to technical limitations. However, both hydrogen and methane remain in the gaseous state, and nitrogen remains in the supercritical state under the conditions used in this study, as they would at full reservoir conditions.

Table 1: Thermophysical properties of fluids at temperature 295K and pressure 100 bar

Fluid	Density kg m <sup>-3</sup>	Viscosity Pa s	Viscosity ratio $M$	Interfacial tension N m <sup>-1</sup>
H <sub>2</sub> [43]	7	9.8 x 10 <sup>-6</sup>	0.01	0.072
CH <sub>4</sub> [44]	61	1.44 x 10 <sup>-5</sup>	0.016	0.05
N <sub>2</sub> [45]	112	1.5 x 10 <sup>-4</sup>	0.16	0.067

Consequently, the findings of this study can be reasonably extended to actual reservoir conditions.

## 2.2. Experimental setup and procedure

The experimental setup is shown in figure 3. Brine and gas are co-injected at increasing gas fractional flows to measure the drainage relative permeability, while keeping the constant total flow rate of 0.1 ml min<sup>-1</sup>. Brine (wetting phase) is delivered using dual syringe Brine pump (Vindum Engineering VP12K). Gas (nonwetting phase) is injected using a syringe Gas pump (ISCO 500D pump). Due to highly flammable nature of hydrogen and methane, the gas pump was stored inside a low-oxygen (< 4 %) safety cabinet. The detailed experimental procedure is as follows:

1. Prior to experimental measurements, the fractured sample was dried in an oven overnight at 40°C. The core was then wrapped in aluminum foil to prevent leakage of hydrogen gas through rubber sleeve.
2. A dry cylindrical fractured rock sample was placed inside a Viton rubber sleeve and loaded in the flow cell.
3. The confining pressure of 15 bar was applied around the sample with deionized water using a high pressure reciprocal Confining pump (Tele-

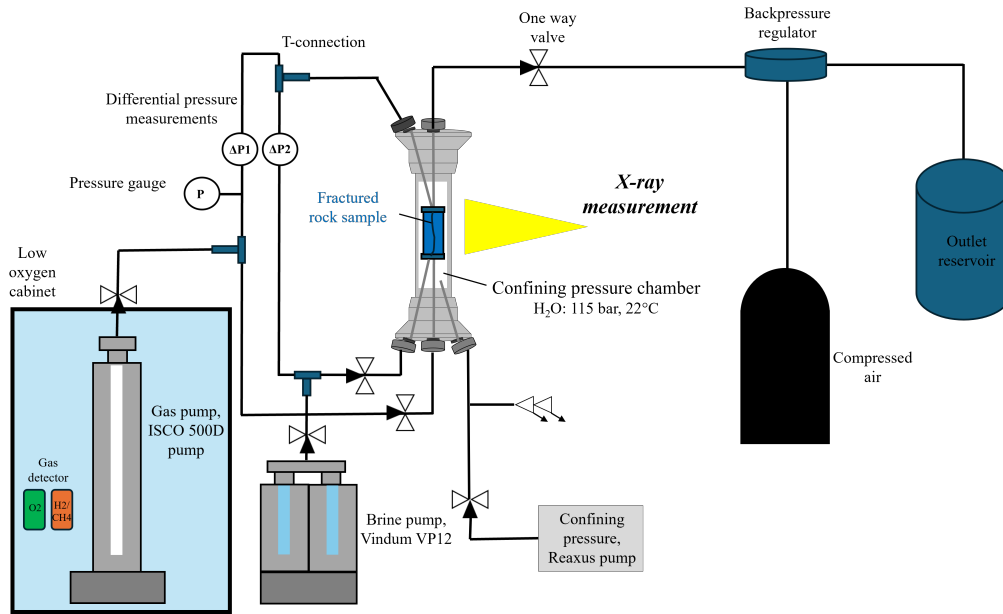


Figure 3: Experimental set-up for two-phase hydrogen/methane/nitrogen-brine core floods performed with X-ray micro computed tomography scanner.

dyne ISCO Reaxus, USA) to secure the sample in position.

4. A dry scan of entire length of the sample was obtained using X-ray CT scanner.
5. 25 wt% potassium iodide (KI) brine solution was injected through the sample at volumetric flow rate of  $5 \text{ ml min}^{-1}$  using Brine pump to saturate the fracture.
6. The flow system was pressurized with KI brine (25 wt%) upto 100 bar while maintaining 15 bar difference between inlet and confining fluid pressures
7. Absolute permeability: The core was flooded with brine at several constant flow rates ranging from  $0.1 \text{ ml min}^{-1}$  to  $1 \text{ ml min}^{-1}$ . Absolute

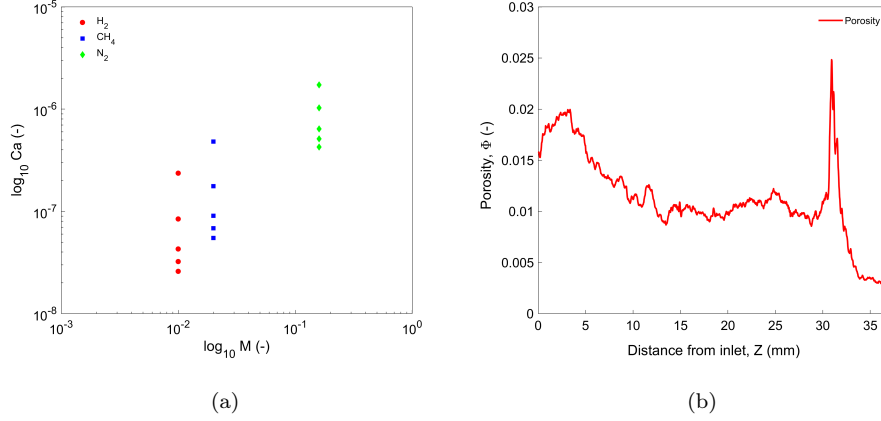


Figure 4: (a) Capillary number ( $Ca_t$ ) and viscosity ratio ( $M$ ) used in this study. (b) Porosity along the length of the core  $\langle \Phi \rangle = 0.011$ .

permeability was then determined using Darcy’s law as described in equation 1. The pressure gradient was monitored at steady-state using a Keller-33PDX pressure transducer. Given the extended duration of the experiments—spanning several days—and the potential for slight alterations in fracture morphology under high-pressure flow conditions, we measured the absolute permeability prior to each set of experiments with different gases. The measured permeability values were 8.5 D for hydrogen, 7.7 D for methane, and 3.5 D for nitrogen.

$$q = -\frac{kA}{\mu} \frac{dP}{L} \quad (1)$$

where,  $q$  is volumetric flow rate,  $k$  is absolute permeability,  $A$  is cross-sectional area of fracture,  $\mu$  is viscosity of the fluid injected,  $dP$  is differential pressure across the sample and  $L$  is the length of sample.

8. The fractional flow of gas is increased from 0.1 to 1 in stepwise manner.

For each fractional flow, sample is scanned after steady-state is reached. The steady-state is confirmed by constant differential pressure across the length of rock sample. Fractional flow of gas is defined by equation 2. The capillary number,  $Ca_t$  for each fractional flow is defined as equation 3 [46] and is given in table 2 for each experiment in this study.

$$f_g = \frac{q_g}{q_g + q_w} \quad (2)$$

where,  $f_g$  is gas fractional flow,  $q_g$  is gas volumetric flow rate and  $q_w$  is brine volumetric flow rate.

$$Ca_t = \frac{q_t}{\sigma \left( \frac{f_g}{\mu_{nw}} + \frac{1-f_g}{\mu_w} \right)} \quad (3)$$

where,  $Ca_t$  is total capillary number at fractional flow during co-injection,  $q_t$  is total volumetric flow rate ( $q_g + q_w$ ),  $\mu_{nw}$  is viscosity of non-wetting phase and  $\mu_w$  is viscosity of wetting phase.

9. Relative permeability: Relative permeability is measured at each fractional flow using equation 4.

$$q_i = - \frac{k k_{r,i}(S_i) A dP}{\mu_i L} \quad (4)$$

where,  $q_i$  is the volumetric flow rate of phase  $i$ ,  $k$  is absolute permeability,  $k_{r,i}(S_i)$  is the relative permeability of phase  $i$ ,  $A$  is the cross-sectional area of fracture,  $\mu_i$  is the viscosity of phase  $i$  and  $dP/L$  is the pressure



Table 2: Capillary number for each fractional flow for different gas-brine systems.

$f_g$	$q_g(\text{ml min}^{-1})$	$q_w(\text{ml min}^{-1})$	$Ca_t \times 10^{-7}$		
			H <sub>2</sub> - brine	CH <sub>4</sub> - brine	N <sub>2</sub> - brine
0.1	0.01	0.09	2.36	4.8	17.2
0.3	0.03	0.07	0.84	1.76	10.28
0.6	0.06	0.04	0.43	0.91	6.41
0.8	0.08	0.02	0.32	0.68	5.12
1.0	0.1	0	0.26	0.55	4.27

gradient.

### 2.3. Imaging and image analysis

X-ray imaging was performed with the ‘High Energy micro-CT Optimized for Research’ scanner (HECTOR) [47] at the center for X-ray tomography at Ghent University (UGCT). The X-ray energy and power were 160 kV and 15 W, respectively. We acquired 1301 projections with 600 ms exposure time for each projection. For each fractional flow at steady state entire sample length is scanned with imaging field of view (FOV) 2000 x 2400 x 1400 voxels. The voxel size was 30.37  $\mu\text{m}$  for each image. The Octopus software (Tescan-XRE, Belgium) was used to reconstruct the 3D image from acquired projections.

The reconstructed images were processed using Avizo (ThermoFisher scientific) software. All the images from wet/fractional flow scans were registered to the dry scan using normalized mutual information and denoised using non-local means filter with similarity value of 0.4. The fracture from the dry scan was segmented using global thresholding, which was then applied as a mask for segmenting the wet or fractional flow scans. Two fluid phases, brine and gas, were segmented from the masked wet images using histogram-based thresholding. The total porosity of the fracture was determined from the

volume fraction of the segmented dry scan, while the saturation of each fluid phase was calculated along the length of the rock sample from the segmented wet scans.

### 3. Results

#### 3.1. Relative permeability

The relative permeability curves were derived directly from stabilized differential pressure and saturation data, as shown in Figure 6. During drainage, as the fractional flow of gas ( $f_g$ ) increases and the capillary number decreases, the system moves to lower water saturations, resulting in better-connected gas-phase displacement. This leads to an increase in gas relative permeability ( $K_{rg}$ ) and a decrease in brine relative permeability ( $K_{rw}$ ). Previous studies report that hydrogen-water systems are water-wet with respect to calcite [48]. In such water-wet systems, gas preferentially invades regions with lower capillary entry pressures during drainage, corresponding to fracture spaces with larger apertures [49, 25, 50]. Figure 5 illustrates gas-brine occupancy at  $f_g = 0.6$  for hydrogen, methane, and nitrogen, where gas is observed occupying largest aperture spaces, while brine prefers to remain in narrower regions. This confirms that this system is water-wet. It is consistent with previous observations in porous media, where gas invades larger pores and brine remains in narrower throats [51]. Similar trends were observed at other fractional flows, as shown in the Supplementary Information S1.

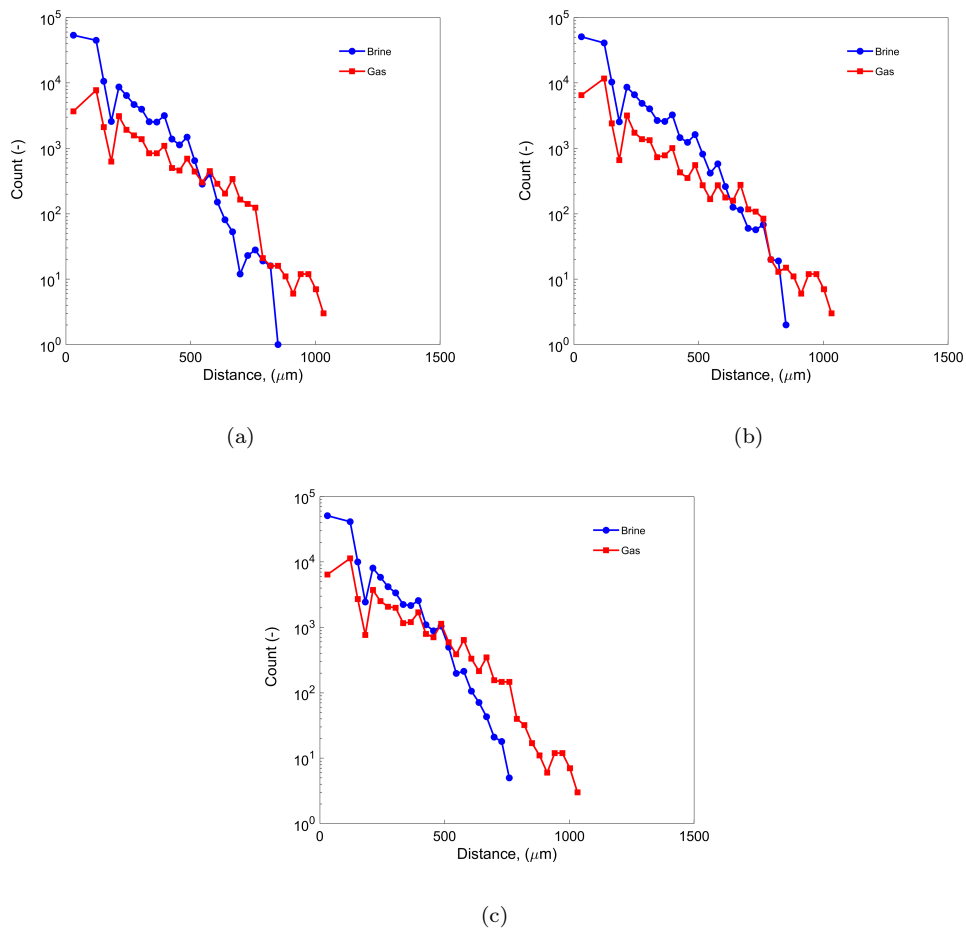


Figure 5: Fluid occupancy at  $f_g = 0.6$  for different gases: (a)  $\text{H}_2$  (b)  $\text{CH}_4$  (c)  $\text{N}_2$ . The distance is derived from the distance map of the segmented dry fracture image, calculated as twice the distance between the center and the nearest wall of the fracture.

The relative permeability-saturation curves for the hydrogen-brine and methane-brine systems show closely aligned trends and similar endpoint saturations. Both gases exhibit low gas relative permeability ( $K_{rg}$ ), indicating substantial phase interference caused by the heterogeneous fracture geometry (roughness) and the low viscosity ratios of the gas-brine systems (0.01 for hydrogen-brine and 0.016 for methane-brine). This behaviour suggests the

occurrence of intermittent flow and snap-off events, further discussed in Section 3.3. The wetting-phase permeability ( $K_{rw}$ ) consistently remains much higher than the gas permeability, indicating that brine stays well-connected across all fractional flows. This strong water-wet condition ensures brine continuity throughout the fracture network, even as gas saturation increases. At higher water saturation (lower fractional flows,  $f_g$ ), the gas relative permeability ( $K_{rg}$ ) is slightly higher for the methane-brine system compared to the hydrogen-brine system. This is attributed to the higher capillary number ( $Ca_t$ ) at high wetting phase saturation, where viscous forces contribute more to the flow dynamics. The slightly higher viscosity ratio of the methane-brine system (0.016 versus 0.01 for hydrogen-brine) facilitates better connectivity in the methane front, resulting in higher gas permeability [46]. However, as the water saturation decreases (e.g.,  $f_g = 0.8$  and  $f_g = 1$ ), capillary forces dominate, leading the  $K_{rg}$  values for hydrogen and methane to converge at similar endpoint saturations  $S_w = 0.6$  for hydrogen and  $S_w = 0.59$  for methane. These slight differences in relative permeability and saturation at endpoints may fall within the experimental margin of error. Notably, the saturation change from  $f_g = 0.1$  to  $f_g = 1$  is identical for both gases, decreasing from 0.91 to 0.6. It should be noted that the entire hydrogen-brine relative permeability experiment was repeated to assess the uncertainty in the measurements and will be discussed in section 3.4.

The nitrogen-brine relative permeability curves show a significant difference from those of hydrogen-brine and methane-brine, specifically with nitrogen maintaining higher gas ( $K_{rg}$ ) and water permeability ( $K_{rw}$ ) across all fractional flows. At the endpoint where water saturation ( $S_w$ ) converges

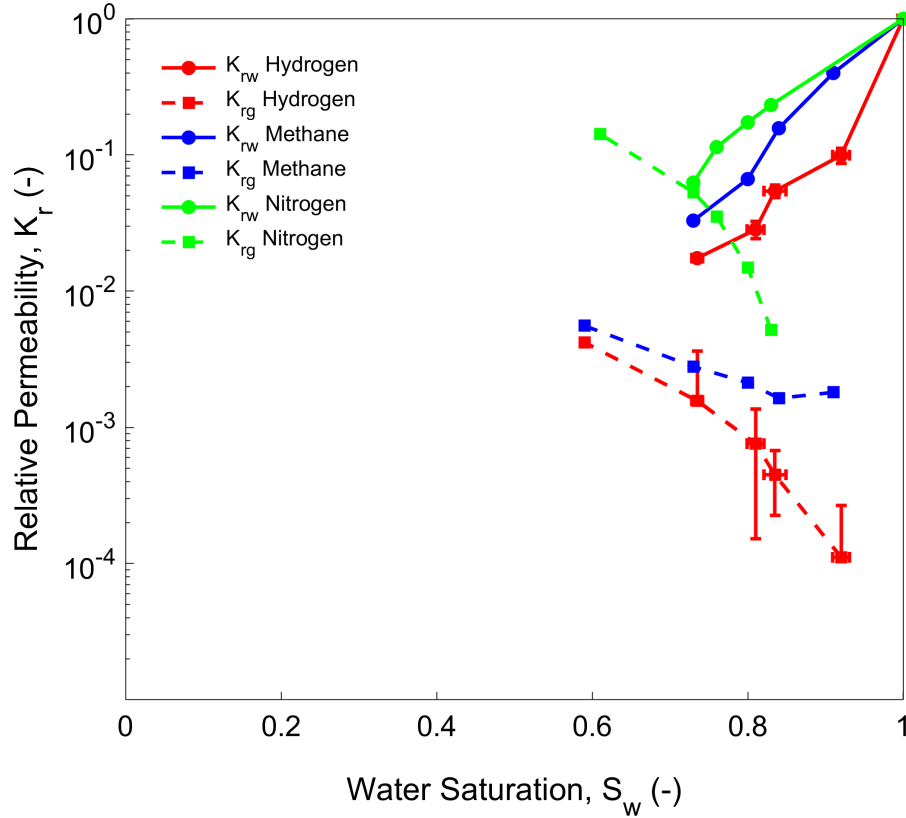


Figure 6: Drainage steady-state relative permeability comparison between hydrogen-brine, methane-brine and nitrogen-brine system at 10 MPa and 22°C.

to 0.6 for all gases, the gas relative permeability ( $K_{rg}$ ) reaches 0.14 for nitrogen, while it is notably lower for hydrogen and methane, at 0.007 and 0.0055, respectively. This difference arises because nitrogen's higher viscosity, an order of magnitude greater than that of hydrogen and methane, increases the capillary number under the same volumetric flow rate conditions. At 10 MPa, nitrogen exists in a supercritical state, which affects its fluid behavior in the fracture system. At the initial fractional flow of  $f_g = 0.1$ , the wetting-phase

saturation for nitrogen is notably lower than that of hydrogen or methane.

### *3.2. Saturation and fluid distribution*

To further explore the cause of the similarities and differences between the different relative permeability measurements, we investigated the average saturation and fluid distribution in the fracture space. The slice-averaged 1-D saturation profiles for hydrogen, methane, and nitrogen experiments at different fractional flows are shown in Figures 7a, 7b, and 8, respectively. As the fractional flow of gas ( $f_g$ ) increases, the slice-averaged brine saturation ( $S_w$ ) across the sample decreases for all gases, indicating that more gas is occupying the fracture space. For hydrogen and methane, saturation varies between 0.3 and 1, while for nitrogen it ranges from 0.27 to 0.99, suggesting a slightly lower average saturation for nitrogen. It results from the fracture geometry being highly heterogeneous with variable aperture distribution and roughness as shown in Figure 2b. The dry scan, Figure 1 reveals secondary fractures branching from the centre of the sample, contributing to the intricate fracture network. This complexity affects the distribution of fluid saturation across the sample, influencing gas displacement efficiency and the overall flow dynamics.

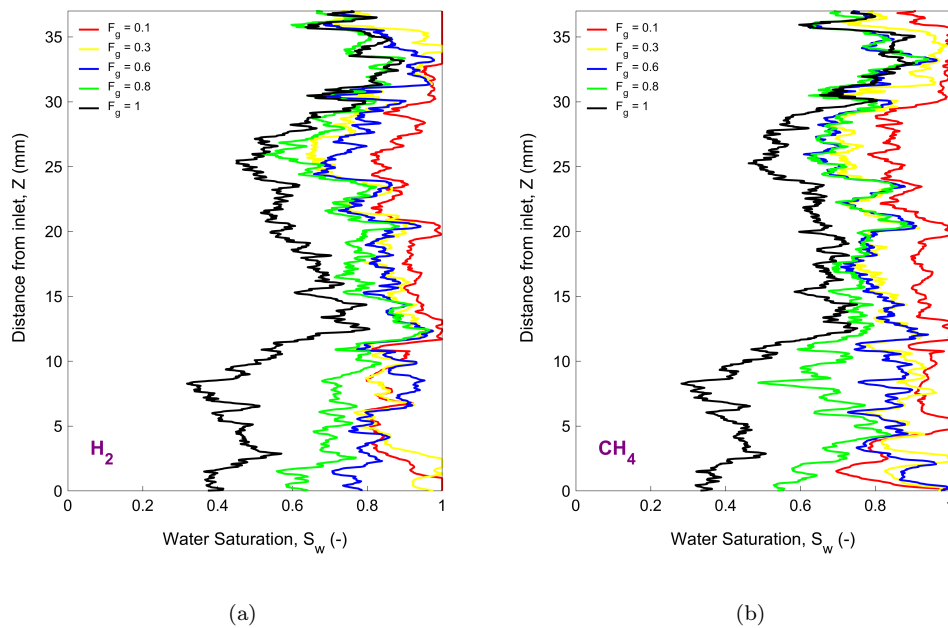


Figure 7: 1-D slice-averaged saturation profile of brine along the length of the core for different gases (a)  $H_2$  (b)  $CH_4$ .

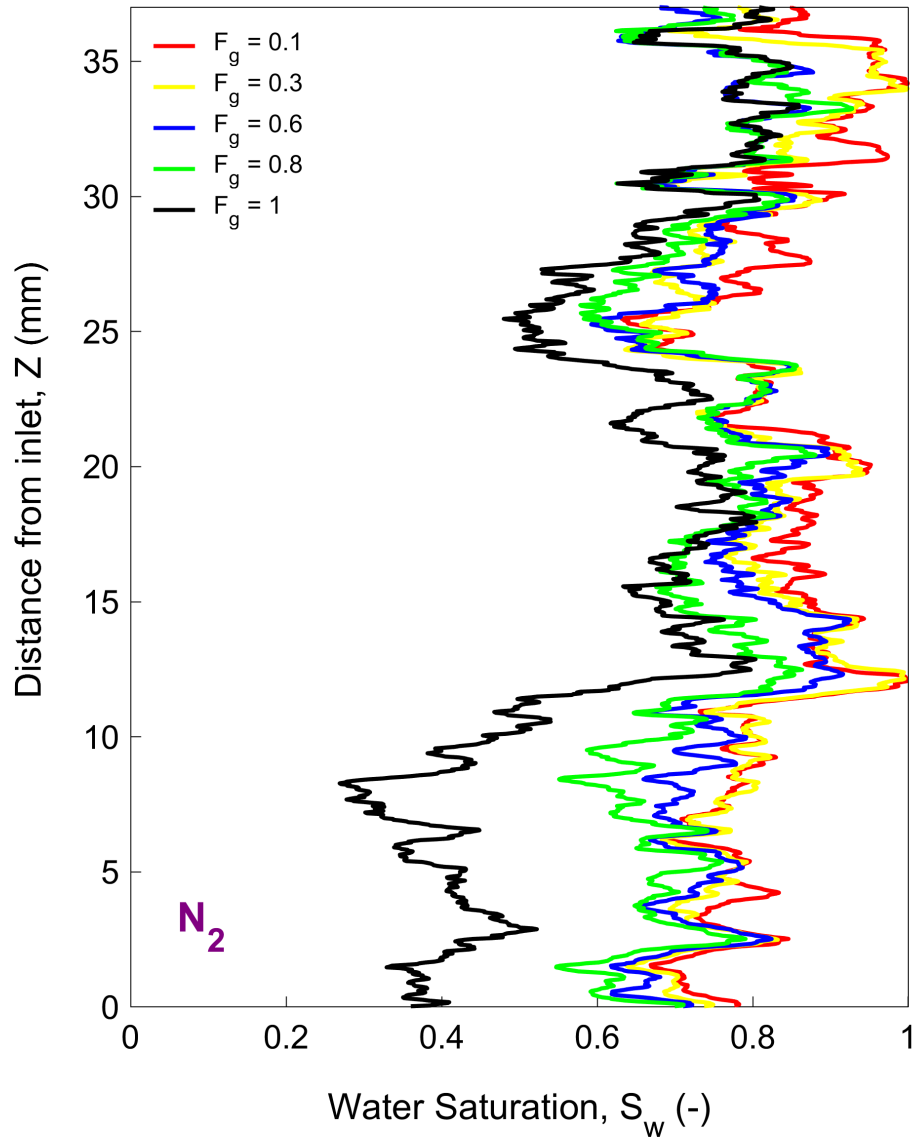


Figure 8: 1-D slice-averaged saturation profile of brine along the length of the core for different fractional flows for  $N_2$ .



At lowest fractional flows  $f_g = 0.1$ , the saturation profiles illustrated in Figure 9a shows noticeable differences, with brine saturation for hydrogen being 5% higher than for methane and 10% higher than for nitrogen. This variation primarily results from hydrogen's lower viscosity, which leads to less efficient invasion of the fractures, ultimately resulting in lower gas saturation and higher wetting-phase saturation. Although the fluid properties of hydrogen and methane at 10 MPa and 22°C are similar, nitrogen, in its supercritical state, demonstrates distinctly different flow behavior. The higher viscosity of nitrogen facilitates more efficient invasion of the fracture network, resulting in higher gas saturation. Nitrogen is observed to drain more efficiently compared to hydrogen and methane in porous media, as also reported by Higgs et al. [36]. Despite the interfacial tension (IFT) of nitrogen ( $0.07 \text{ N m}^{-1}$ ) and hydrogen ( $0.069 \text{ N m}^{-1}$ ) being comparable at 10 MPa, the differences in viscosity significantly influence wetting-phase saturation at onset of drainage. This underscores the finding that at low fractional flows, the viscosity ratio plays a more pronounced role in gas displacement behavior. The fluid distribution in the fracture at  $f_g = 0.6$ , as shown in Figure 10, indicates that nitrogen has the highest gas fraction ( $S_w = 0.76$ ) in the fracture, followed by methane ( $S_w = 0.8$ ), and then hydrogen ( $S_w = 0.76$ ).

At higher gas fractional flows ( $f_g = 0.8$  and 1) the saturation converges for all gases as shown in Figure 9b. At these higher gas fractional flows, the capillary number decreases resulting in more connected gas which diminishes the impact of the viscosity ratio. Consequently, similar saturations are observed at  $f_g = 1$ , representing endpoint saturation. Although the nitrogen case has a significantly higher Ca ( $1.2 \times 10^{-6}$ ) than hydrogen and methane

( $7.0 \times 10^{-6}$  and  $1.5 \times 10^{-6}$  respectively), the end point saturations remain consistent for all gases at  $S_w = 0.6$ . This suggests that the effect of capillary number on overall saturation is relatively minor under the tested conditions.

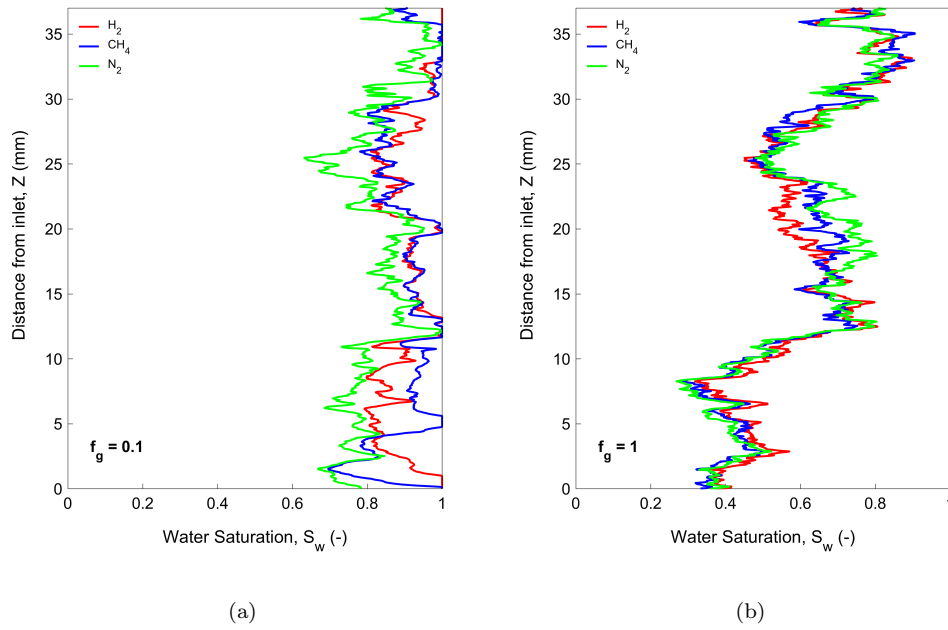


Figure 9: 1-D slice-averaged saturation profile of brine along the length of the core for different gases (a)  $f_g = 0.1$  (b)  $f_g = 1$ .

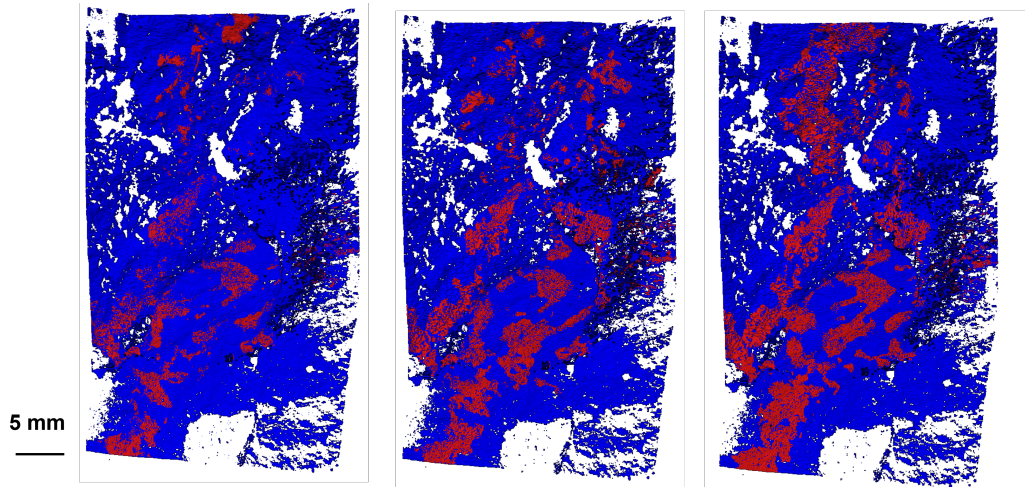


Figure 10: Fluid distribution in the fracture at  $f_g=0.6$  (left)  $H_2$ , (middle)  $CH_4$ , (right)  $N_2$ .

The fluid distribution for the hydrogen-brine system in the fracture exhibits signs of intermittency at higher water saturations (lower  $f_g$ ), as illustrated in Figure 11 for  $f_g = 0.1$ . Subtle differences in gas distribution are observed between two scans taken 30 minutes apart after reaching steady-state pressure. Several locations are identified by coloured circles: Circle 1 (yellow) marks a region where gas disappears in the subsequent scan, while Circles 2 (green) indicate location where gas reappears. These fluctuations in the gas phase correspond to capillary events and are also reflected in the measured differential pressure. In contrast, the nitrogen-brine system exhibits fewer fluctuations in saturation, suggesting a more stable flow pattern. A more detailed analysis of pressure fluctuations, intermittency, and their impact on fluid distribution will be discussed in Section 3.3. Along the length of the fracture, slice-averaged saturation reaches  $S_w = 1$  for many slices, indicating a disconnected gas phase. Figure 12 presents the 1-D slice-averaged saturation profiles for these two subsequent scans revealing significant fluctuations

in saturation within this period, emphasizing dynamic capillary processes occurring in the fracture. These processes are not fully captured in terms of intermediate gray values due to the scanner’s limited temporal resolution. As the gas fractional flow increases to  $f_g = 0.8$ , the gas phase becomes more connected throughout the fracture, which reduces intermittency and enhances overall gas saturation as demonstrated by the 3D volume rendering of fluid distribution in Figure 13. Intermittency significantly impacts relative permeability, resulting in notably low gas permeabilities, particularly for hydrogen and methane as discussed in Section 3.1.

We note here that the observed intermittency may also be influenced by the dissolution of hydrogen and methane into the brine during the experiment, as the injected gas and brine were not pre-equilibrated, a phenomenon previously described by [33]. However, the reappearance of gas in the fracture downstream indicates that intermittency is a genuine effect and not solely attributed to dissolution. The solubilities of hydrogen, methane, and nitrogen in water are  $0.8 \text{ mg L}^{-1}$ ,  $22.7 \text{ mg L}^{-1}$ , and  $10 \text{ mg L}^{-1}$ , respectively. Hydrogen’s significantly lower solubility, yet comparable phase disconnectivity, suggests that dissolution effects are likely minimal.

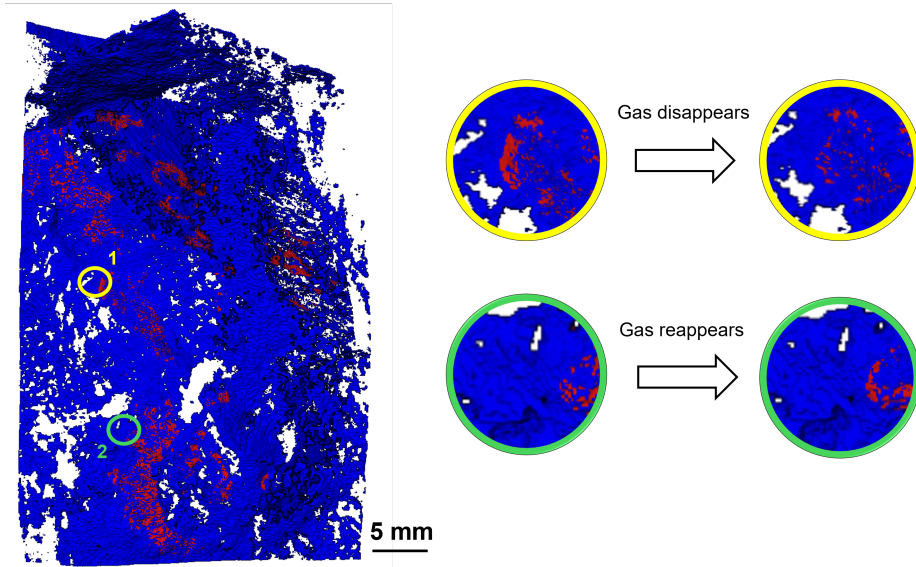


Figure 11: Fluid distribution in fracture of hydrogen-brine flow at  $f_g = 0.1$  for two scans taken 30 minutes apart.

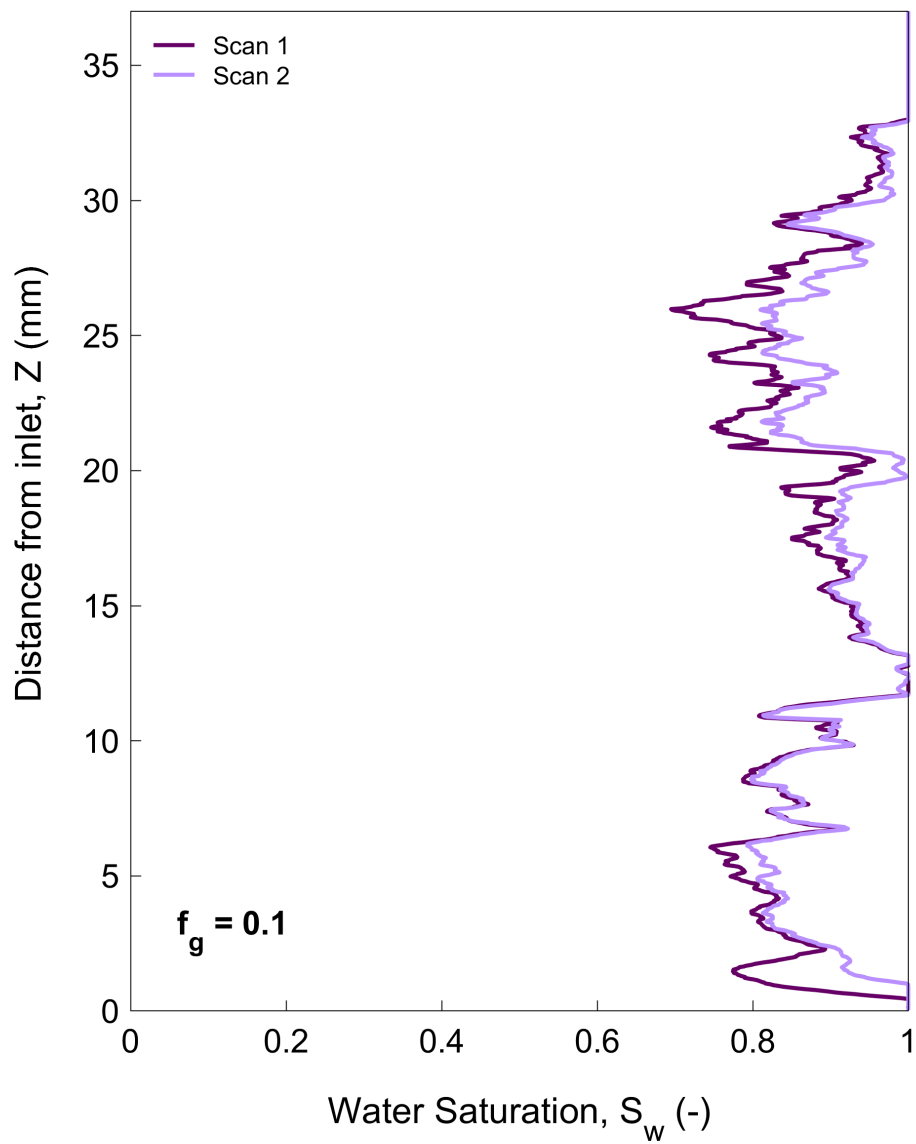


Figure 12: 1-D slice-averaged saturation profile of hydrogen-brine flow at  $f_g = 0.1$  for two scans taken 30 minutes apart.

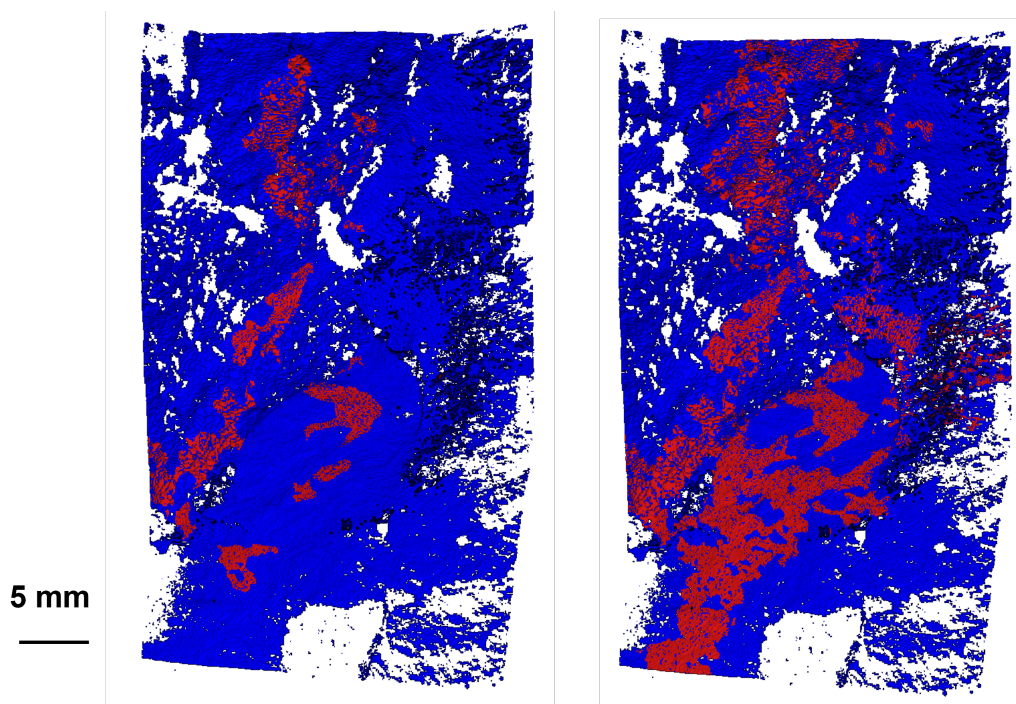


Figure 13: H<sub>2</sub>-brine distribution in the fracture (left)  $f_g = 0.1$  (right)  $f_g = 0.8$ .

### 3.3. Pressure analysis

The lower gas relative permeabilities for similar global water saturation suggest higher phase interference in the fracture. Saturation and fluid distribution in the fracture, based on scans taken 30 minutes apart, indicate the presence of intermittency, where Haines jumps and snap-off events occur. Since the scan duration is 16 minutes and these events appear to happen much more rapidly, we observed pressure data recorded at a much higher time resolution of 1 second. The fluctuations in differential pressure measurements from the transducer across the rock samples provide insights into the timescale and the fluctuations that correspond to snap-off and Haines jumps occurring during two-phase displacements [52, 51]. Differential pres-

sure measurements at  $f_g = 0.6$  over a 30-minute period for H<sub>2</sub>, CH<sub>4</sub>, and N<sub>2</sub> are presented in Figure 14. These data reveal fluctuations over varied timescales for each gas, underscoring distinct dynamics associated with each gas phase. There are notable differences in the amplitude and frequency of these oscillations, particularly between H<sub>2</sub> and CH<sub>4</sub> on one hand and N<sub>2</sub> on the other. The pressure amplitude of fluctuations is greater for hydrogen and methane compared to nitrogen, with the fluctuations occurring over timescales of approximately 150 seconds for hydrogen, 30 seconds for methane, and one second for nitrogen. The pressure fluctuations within the pores result in intermittent pore filling, occurring over a broad range of timescales. At different fractional flows, the timescales of these fluctuations vary, reflecting changes in the connectivity of the gas phase. The additional pressure data and preliminary analysis, including the Gaussian distribution of fluctuations and red noise, are provided in Supplementary Information S2.



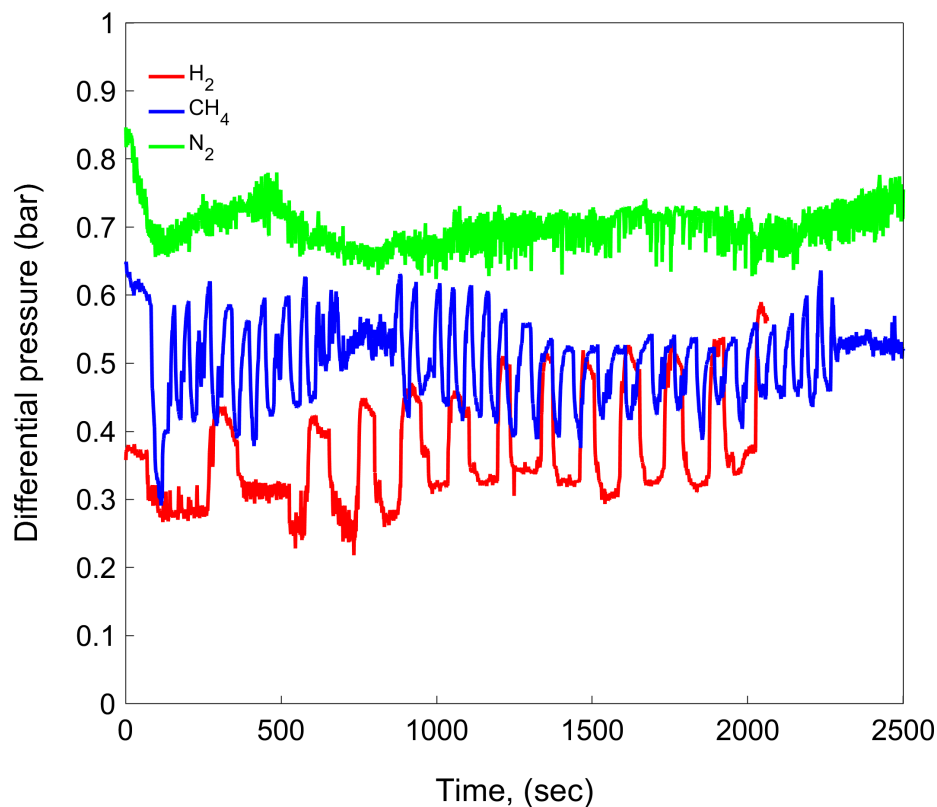


Figure 14: Differential pressure data during steady-state for  $f_g = 0.6$ .

### 3.4. Sensitivity analysis

As discussed in previous sections, relative permeabilities at reservoir conditions in fractures are strongly influenced by intermittency, leading to significant fluctuations in pressure and saturation. To assess the sensitivity of the hydrogen-brine system under these conditions, we repeated the experiment under identical flow conditions. Overall, qualitative trends in the relative permeability-saturation curves remained consistent across both runs, as shown in Figure 15. The water permeabilities ( $K_{rw}$ ) were quantitatively

similar in both runs. Gas permeability, while consistently low across runs, exhibited slight differences, likely due to minor pressure fluctuation variations. Since gas permeabilities are very low, even slight variations in pressure fluctuations can result in differences in the measured relative gas permeability. The pressure fluctuations for these two runs at  $f_g = 0.6$  are shown in Figure 15b. The data clearly exhibits cyclic fluctuations, with the timescales of these fluctuations differing between the two runs: in the first run, the period was 0.5 minutes, while in the repeated run, the period extended to 2.5 minutes. These variations in fluctuation timescales may contribute to slight differences in the calculated relative gas permeabilities. Such differences could arise due to slight changes in fracture morphology, potentially occurring during pressurization, as the fracture is sensitive to applied stress. Over the course of running different experiments presented in this paper, the rock sample underwent pressurization-depressurization cycles, potentially impacting fracture morphology. This is reflected in the observed decrease in absolute permeability before the experimental runs, from 23 D to 8 D. Despite these slight variations, the overall behavior remains consistent across both experimental runs, confirming that our workflow is robust and validating the results presented in this study. The differential pressure data for other fractional flows are provided in Supplementary Information S3.

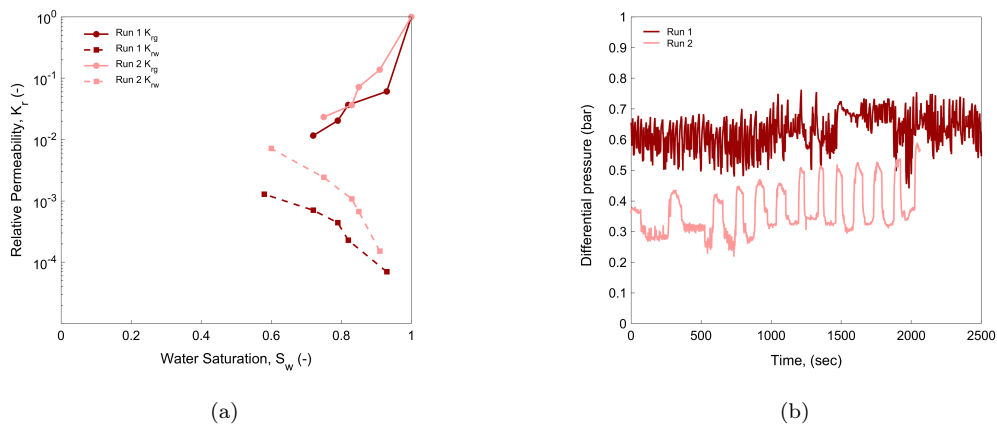


Figure 15: (a) Relative permeability of hydrogen-brine system for two runs. (b) Differential pressure recorded over 30 minutes for two runs of hydrogen-brine experiment.

#### 4. Discussion

Direct measurements of relative permeability for hydrogen compared to other gases in fractured rock samples are currently absent from the literature. Here, we compare our findings with existing experimental data and numerical models for different fluid systems in rough fractures, as shown in Figure 16. Compared to previous studies, the hydrogen gas relative permeability in our system is notably lower, indicating interference effects that are stronger than predicted by existing models such as [27], Gong et al. [29], and Bertels et al. [53]. The limited available experimental data were collected under different flow conditions and using different fluids, making direct comparisons challenging. The fluid pairs used in various studies from the literature are summarized in Supplementary Information S4. The nitrogen permeability aligns more closely with the model proposed by Gong et al. [29]; however, the impact of fracture geometry could not be fully resolved based on these

comparisons. The nitrogen-brine system relative permeabilities were also compared to models from the literature, with detailed discussions provided in the Supplementary Information S4. In contrast, water permeability in our results aligns more closely with the model suggested by Piri and Karpyn [54]. Importantly, fracture morphology also influences these differences, so while such comparisons are informative, they are not definitive. Controlled experiments and models that account for specific fracture morphology in hydrogen-brine systems are essential for more conclusive insights.

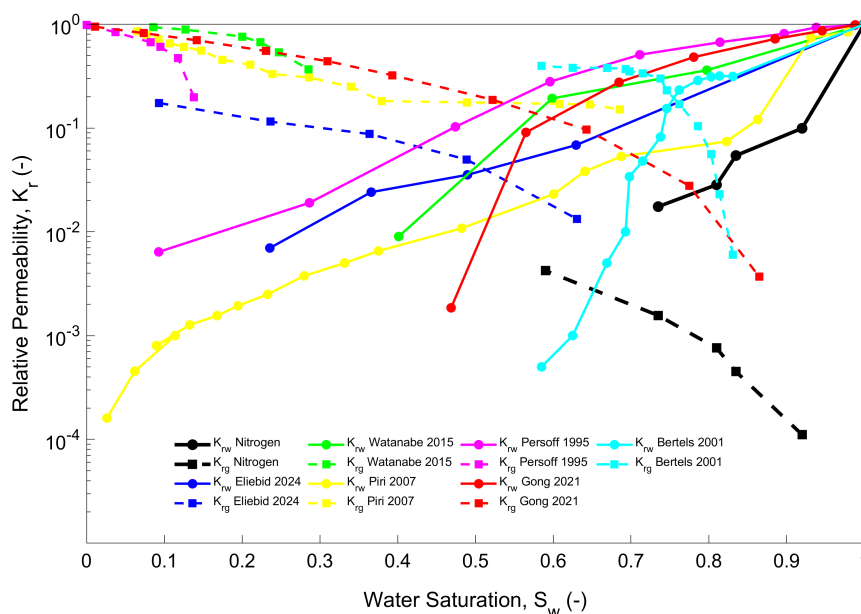


Figure 16: Comparison of relative permeability measurements with previous studies in fracture.

The lower hydrogen gas permeability observed in our fracture study is consistent with trends seen in porous media; thus, we also compared our measurements with direct hydrogen permeability data from porous media studies

in Berea sandstone [32, 33] and Bentheimer sandstone [36], shown in Figure 17. Despite marked differences in sample geometry and flow conditions, the results remain qualitatively comparable, as all experiments were conducted at low capillary numbers ( $Ca_t$ ). In porous media, the relative permeability curves from Higgs et al. [36] exhibit closer alignment for hydrogen, methane, and nitrogen. However, our fracture study reveals greater differences in both wetting- and non-wetting-phase permeabilities. This divergence can likely be attributed to the increased intermittency in the fracture, resulting from the higher pressure conditions (100 bar) in our study, where the interfacial tension (IFT) between hydrogen and methane differs more significantly, and nitrogen exists in a supercritical state. In contrast, the experiments by Higgs et al. [36], conducted at 20 bar, were performed under conditions where the fluid properties of these gases were more similar. Additionally, our study shows a much higher irreducible saturation, exemplifying the dependence of capillary-dominated relative permeability curves on flow rate (injection rate) and geometry (porous vs. fractured). When comparing our hydrogen permeability results to those from Boon and Hajibeygi [33], who also conducted high-pressure experiments (100 bar) at 18°C under similar conditions, hydrogen and water permeabilities were generally higher across most saturations for porous media, though the general trend remains consistent. These comparisons highlight the increased complexity of fluid interactions in fractures compared to those observed in porous media.

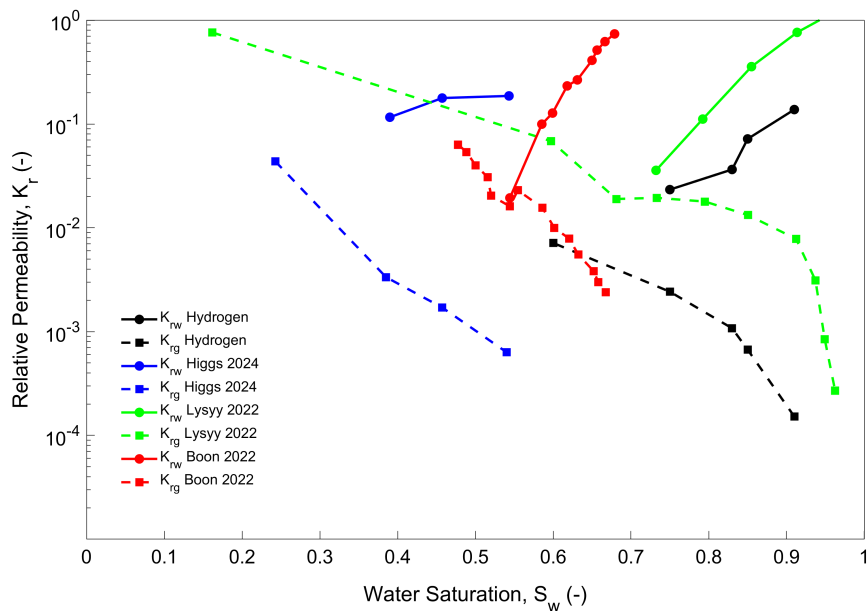


Figure 17: Comparison of relative permeability measurements with previous hydrogen measurement studies in porous media. The black lines denote the hydrogen-brine data from our study.

## 5. Conclusions

The findings from our hydrogen-brine and methane-brine experiments, along with nitrogen-brine experiment, provide crucial insights for hydrogen storage in subsurface fractured reservoirs and particularly in the case of transitioning existing natural gas storage facilities. Our experiments are focused on the Loenhout storage site in northern Belgium which is a part of the Be-HyStore project. We conducted direct measurements of hydrogen, methane, and nitrogen relative permeabilities in fractured rock under reservoir pressure conditions (10 MPa), while recognizing that experimental limitations prevented matching the reservoir temperature. However, the impact of tem-

perature on relative permeability is expected to be minimal.

Our study summarizes three key findings relevant to hydrogen storage in fractured reservoirs:

1. The fracture relative permeability curves for hydrogen and methane are similar, suggesting that similar intrinsic flow properties would be maintained after repurposing the storage from natural gas to hydrogen. The minor differences observed are attributed to methane's higher viscosity and lower interfacial tension ( $0.05 \text{ N m}^{-1}$  for methane versus  $0.07 \text{ N m}^{-1}$  for hydrogen).
2. Relative permeability for both hydrogen and methane in fractured rocks is low, with substantial phase interference caused by flow intermittency. This behavior is not well represented by existing models, highlighting the need for more advanced modeling approaches to accurately capture the dynamics of hydrogen and methane in fractured media.
3. Nitrogen exhibits significantly higher gas relative permeability, making it unsuitable as a laboratory proxy. It also influences considerations for its use as a cushion gas due to its propensity for breakthrough issues during injection and production.

In underground gas storage, tight shale caprock typically acts as a barrier, but fractures, whether preexisting or induced by pressure variations during hydrogen injection, can provide additional pathways for gas movement. The low gas relative permeability observed in this study may contribute to the mitigation of leakage risks supporting the long-term stability and security of hydrogen storage.

In conclusion, this study provides critical insights into hydrogen behavior in fractured rock, supporting efforts to optimize underground hydrogen storage. By highlighting the limitations of using nitrogen as a proxy for hydrogen, our findings emphasize the need for hydrogen-specific research to develop effective storage strategies and safety protocols in subsurface reservoirs.

Future work should focus on measuring hydrogen-brine relative permeability in fracture samples with varied aperture sizes and roughness. Such studies will be valuable in understanding the impact of fracture geometry on flow behavior, ultimately enhancing the accuracy of upscaled fracture network models for reservoir-scale applications.

## Acknowledgments

This study was financed in part by Fluxys, Belgium. We also acknowledge research funding from the Belgian Federal Energy Transition Fund (project BE-HyStore), the Research Foundation-Flanders (FWO, project G004820N and G51418N) and Ghent University's Special Research Fund (BOF/COR/2022/008). We gratefully acknowledge Prof. Kamaljit Singh and Zaid Jangda (Heriot-Watt University) for their advice on designing our hydrogen flow setup.

## References

- [1] Radoslaw Tarkowski. Underground hydrogen storage: Characteristics and prospects. *Renewable and Sustainable Energy Reviews*, 105 (January):86–94, 2019. doi: <https://doi.org/10.1016/j.rser.2019.01.051>.



- [2] Cevahir Tarhan and Mehmet Ali Çil. A study on hydrogen, the clean energy of the future: Hydrogen storage methods. *Journal of Energy Storage*, 40:102676, 2021. doi: <https://doi.org/10.1016/j.est.2021.102676>.
- [3] Davood Zivar, Sunil Kumar, and Jalal Foroozesh. Underground hydrogen storage: A comprehensive review. *International Journal of Hydrogen Energy*, 46(45):23436–23462, 2021. doi: <https://doi.org/10.1016/j.ijhydene.2020.08.138>.
- [4] Sugan Raj Thiyagarajan, Hossein Emadi, Athar Hussain, Prathamesh Patange, and Marshall Watson. A comprehensive review of the mechanisms and efficiency of underground hydrogen storage. *Journal of Energy Storage*, 51:104490, 2022. doi: <https://doi.org/10.1016/j.est.2022.104490>.
- [5] Manal Al-Shafi, Osama Massarweh, Ahmad S. Abushaikha, and Yusuf Bicer. A review on underground gas storage systems: Natural gas, hydrogen and carbon sequestration. *Energy Reports*, 9:6251–6266, 2023. doi: <https://doi.org/10.1016/j.egy.2023.05.236>.
- [6] M. S.A. Perera. A review of underground hydrogen storage in depleted gas reservoirs: Insights into various rock-fluid interaction mechanisms and their impact on the process integrity. *Fuel*, 334(P1):126677, 2023. doi: <https://doi.org/10.1016/j.fuel.2022.126677>.
- [7] Canan Acar and Ibrahim Dincer. Comparative assessment of hydrogen production methods from renewable and non-renewable sources. *In-*

- ternational Journal of Hydrogen Energy*, 39(1):1–12, 2014. doi: <http://dx.doi.org/10.1016/j.ijhydene.2013.10.060>.
- [8] Andrew Cavanagh, Hamid Yousefi, Mark Wilkinson, and Remco Groenenberg. Hydrogen storage potential of existing european gas storage sites in depleted gas fields and aquifers. Technical report, June 2022.
- [9] Roland Dreesen, Jos Bouckaert, Michiel Duser, J Soille, and Noël Vandenberghe. Subsurface structural analysis of the late-Dinantian carbonate shelf at the northern flank of the Brabant Massif (Campine Basin, N-Belgium). *Mémoires pour servir à l'Explication des Cartes Géologiques et Minières de la Belgique*, 21:1–37, 1987.
- [10] David Lagrou and Ben Laenen. Introduction of new formal lithographic units for the Dinantian in the Campine Basin. In *In Proceedings of the 4th International Geologica Belgica Meeting*, pages 11–14, 2012.
- [11] Noël Vandenberghe, Mieke De Craen, and Koen Beerten. Geological framework of the Campine Basin. Geological setting, tectonics, sedimentary sequences. *External Report of the Belgian Nuclear Research Centre*, ER-262:1–112, 2014. doi: <http://hdl.handle.net/10038/8544>.
- [12] Niklas Heinemann, Juan Alcalde, Johannes M. Miocic, Suzanne J.T. Hangx, Jens Kallmeyer, Christian Ostertag-Henning, Aliakbar Hassanpouryouzband, Eike M. Thaysen, Gion J. Strobel, Cornelia Schmidt-Hattenberger, Katriona Edlmann, Mark Wilkinson, Michelle Bentham, R. Stuart Haszeldine, Ramon Carbonell, and Alexander Rudloff. Enabling large-scale hydrogen storage in porous media-the scientific chal-

- lenges. *Energy and Environmental Science*, 14(2):853–864, 2021. doi: <https://doi.org/10.1039/D0EE03536J>.
- [13] Maksim Lysyy, Martin Fernø, and Geir Ersland. Seasonal hydrogen storage in a depleted oil and gas field. *International Journal of Hydrogen Energy*, 46(49):25160–25174, 2021. doi: <https://doi.org/10.1016/j.ijhydene.2021.05.030>.
- [14] Adnan Aftab, Aliakbar Hassanpouryouzband, Quan Xie, Laura L. Machuca, and Mohammad Sarmadivaleh. Toward a Fundamental Understanding of Geological Hydrogen Storage. *Industrial and Engineering Chemistry Research*, 61(9):3233–3253, 2022. doi: <https://doi.org/10.1021/acs.iecr.1c04380>.
- [15] Masoud Aslannezhad, Muhammad Ali, Azim Kalantariasl, Mohammad Sayyafzadeh, Zhenjiang You, Stefan Iglauer, and Alireza Keshavarz. A review of hydrogen/rock/brine interaction: Implications for Hydrogen Geo-storage. *Progress in Energy and Combustion Science*, 95:101066, 2023. doi: <https://doi.org/10.1016/j.pecs.2022.101066>.
- [16] Martin J. Blunt. *Multiphase flow in permeable media: a pore-scale perspective*. Cambridge university press. doi: <https://doi.org/10.1017/9781316145098>.
- [17] Tomos Phillips, Niko Kampman, Kevin Bisdom, Nathaniel D. Forbes Inskip, Sabine A.M. den Hartog, Veerle Cnudde, and Andreas Busch. Controls on the intrinsic flow properties of mudrock fractures: A review

- of their importance in subsurface storage. *Earth-Science Reviews*, 21: 103390, 2020. doi: <https://doi.org/10.1016/j.earscirev.2020.103390>.
- [18] K. Pruess and Y. W. Tsang. On two-phase relative permeability and capillary pressure of rough-walled rock fractures. *Water Resources Research*, 26(9):1915–1926, 1990. doi: <https://doi.org/10.1029/WR026i009p01915>.
- [19] P. Persoff and K. Pruess. Two-Phase Flow Visualization and Relative Permeability Measurement in Natural Rough-Walled Rock Fractures. *Water Resources Research*, 31(5):1175–1186, 1995. doi: <https://doi.org/10.1029/95WR00171>.
- [20] Chih Ying Chen and Roland N. Horne. Two-phase flow in rough-walled fractures: Experiments and a flow structure model. *Water Resources Research*, 42(3):1–17, 2006. doi: <https://doi.org/10.1029/2004WR003837>.
- [21] Da Huo and Sally M. Benson. Experimental Investigation of Stress-Dependency of Relative Permeability in Rock Fractures. *Transport in Porous Media*, 113(3):567–590, 2016. doi: <https://doi.org/10.1007/s11242-016-0713-z>.
- [22] M J Nicholl, H Rajaram, and R J Glass. Factors controlling saturated relative permeability in a partially saturated horizontal fracture. 27(3): 393–396, 2000.
- [23] Zhibing Yang, Auli Niemi, Fritjof Fagerlund, and Tissa Illangasekare. Two-phase flow in rough-walled fractures: Comparison of continuum

- and invasion-percolation models. *Water Resources Research*, 49(2):993–1002, 2013. doi: <https://doi.org/10.1002/wrcr.20111>.
- [24] Zuyang Ye, Hui Hai Liu, Qinghui Jiang, and Chuangbing Zhou. Two-phase flow properties of a horizontal fracture: The effect of aperture distribution. *Advances in Water Resources*, 76:43–54, 2015. doi: <http://dx.doi.org/10.1016/j.advwatres.2014.12.001>.
- [25] Tomos Phillips, Tom Bultreys, Jeroen van Stappen, Kamaljit Singh, Erik Clemens Boersheim, Sahyuo Achuo Dze, Stefanie von Offenwert, Ben Callow, Mostafa Borji, Vladimir Novak, Christian M. Schlepütz, Veerle Cnudde, Florian Doster, and Andreas Busch. Influence of Local Aperture Heterogeneity on Invading Fluid Connectivity During Rough Fracture Drainage. *SSRN Electronic Journal*, 151:2387–2403, 2023. doi: <https://doi.org/10.1007/s11242-024-02117-5>.
- [26] Sobhan Hatami and Stuart D.C. Walsh. Relative permeability of two-phase flow through rough-walled fractures: Effect of fracture morphology and flow dynamics. *Journal of Hydrology*, 613(Part B):128326, 2022. doi: <https://doi.org/10.1016/j.jhydrol.2022.128326>.
- [27] Noriaki Watanabe, Keisuke Sakurai, Takuya Ishibash, Yutaka Ohsaki, Tetsuya Tamagawa, Masahiko Yagi, and Noriyoshi Tsuchiya. New m-type relative permeability curves for two-phase flows through subsurface fractures. *JAWRA Journal of the American Water Resources Association*, 51(4):2807–2824, 2015. doi: <https://doi.org/10.1002/2014WR016515>.

- [28] Lichun Wang and M. Bayani Cardenas. Connecting Pressure-Saturation and Relative Permeability Models to Fracture Properties: The Case of Capillary-Dominated Flow of Supercritical CO<sub>2</sub> and Brine. *Water Resources Research*, 54(9):6965–6982, 2018. doi: <https://doi.org/10.1029/2018WR023526>.
- [29] Yanbin Gong, Mohammad Sedghi, and Mohammad Piri. Two-Phase Relative Permeability of Rough-Walled Fractures: A Dynamic Pore-Scale Modeling of the Effects of Aperture Geometry. *Water Resources Research*, 57(12), 2021. doi: <https://doi.org/10.1029/2021WR030104>.
- [30] Mohammed Eliebid, Abdelhalim Mohamed, Maziar Arshadi, Yanbin Gong, and Mohammad Piri. Relative permeability hysteresis and residual trapping in rough-walled fractures: An experimental investigation of the effects of flow rate and saturation history using the steady-state approach. *Advances in Water Resources*, 189:104729, 2024. doi: <https://doi.org/10.1016/j.advwatres.2024.104729>.
- [31] A. E. Yekta, J. C. Manceau, S. Gaboreau, M. Pichavant, and P. Audigane. Determination of Hydrogen–Water Relative Permeability and Capillary Pressure in Sandstone: Application to Underground Hydrogen Injection in Sedimentary Formations. *Transport in Porous Media*, 122(2):333–356, 2018. doi: <https://doi.org/10.1007/s11242-018-1004-7>.
- [32] Maksim Lysyy, Tore Føyen, Else Birkeland Johannesen, Martin Fernø, and Geir Ersland. Hydrogen Relative Permeability Hysteresis in Underground Storage. *Geophysical Research Letters*, 49(17):e2022GL100364, 2022. doi: <https://doi.org/10.1029/2022GL100364>.

- [33] Maartje Boon and Hadi Hajibeygi. Experimental characterization of H<sub>2</sub>/water multiphase flow in heterogeneous sandstone rock at the core scale relevant for underground hydrogen storage (UHS). *Scientific Reports*, 12(1):1–12, 2022. doi: <https://doi.org/10.1038/s41598-022-18759-8>.
- [34] Zaid Jangda, Hannah Menke, Andreas Busch, Sebastian Geiger, Tom Bultreys, Helen Lewis, and Kamaljit Singh. Pore-scale visualization of hydrogen storage in a sandstone at subsurface pressure and temperature conditions: Trapping, dissolution and wettability. *Journal of Colloid and Interface Science*, 629(Part B):316–325, 2023. doi: <https://doi.org/10.1016/j.jcis.2022.09.082>.
- [35] Scott Higgs, Ying Da Wang, Chenhao Sun, Jonathan Ennis-King, Samuel J. Jackson, Ryan T. Armstrong, and Peyman Mostaghimi. Direct measurement of hydrogen relative permeability hysteresis for underground hydrogen storage. *International Journal of Hydrogen Energy*, 50 (Part D):524–541, 2024. doi: <https://doi.org/10.1016/j.ijhydene.2023.07.270>.
- [36] Scott Higgs, Ying Da Wang, Chenhao Sun, Jonathan Ennis-King, Samuel J. Jackson, Ryan T. Armstrong, and Peyman Mostaghimi. Comparative analysis of hydrogen, methane and nitrogen relative permeability: Implications for Underground Hydrogen Storage. *Journal of Energy Storage*, 73(Part C):108827, 2023. doi: <https://doi.org/10.1016/j.est.2023.108827>.
- [37] Zhenkai Bo, Maartje Boon, Hadi Hajibeygi, and Suzanne Hurter. Impact of experimentally measured relative permeability hysteresis on reservoir-

- scale performance of underground hydrogen storage (UHS). *International Journal of Hydrogen Energy*, 48(36):13527–13542, 2023. doi: <https://doi.org/10.1016/j.ijhydene.2022.12.270>.
- [38] Amin Rezaei, Aliakbar Hassanpouryouzband, Ian Molnar, Zeinab Derikvand, R. Stuart Haszeldine, and Katriona Edlmann. Relative Permeability of Hydrogen and Aqueous Brines in Sandstones and Carbonates at Reservoir Conditions. *Geophysical Research Letters*, 49(12):e2022GL099433, 2022. doi: <https://doi.org/10.1029/2022GL099433>.
- [39] Leila Hashemi, Martin Blunt, and Hadi Hajibeygi. Pore-scale modelling and sensitivity analyses of hydrogen-brine multiphase flow in geological porous media. *Scientific Reports*, 11(1):1–13, 2021. doi: <https://doi.org/10.1038/s41598-021-87490-7>.
- [40] Mohammad Zamehrian and Behnam Sedaei. Underground hydrogen storage in a partially depleted gas condensate reservoir: Influence of cushion gas. *Journal of Petroleum Science and Engineering*, 212:110304, 2022. doi: <https://doi.org/10.1016/j.petrol.2022.110304>.
- [41] Eva van der Voet, Philippe Muchez, Ben Laenen, Gert Jan Weltje, David Lagrou, and Rudy Swennen. Characterizing carbonate reservoir fracturing from borehole data – A case study of the Viséan in northern Belgium. *Marine and Petroleum Geology*, 111:375–389, 2020. doi: <https://doi.org/10.1016/j.marpetgeo.2019.08.040>.
- [42] Jeff Gostick, Zohaib Khan, Thomas Tranter, Matthew Kok, Mehrez Agnaou, Mohammadamin Sadeghi, and Rhodri Jervis. PoreSpy: A Python



- Toolkit for Quantitative Analysis of Porous Media Images. *Journal of Open Source Software*, 4(37):1296, 2019. doi: <https://doi.org/10.21105/joss.01296>.
- [43] Mirhasan Hosseini, Jalal Fahimpour, Muhammad Ali, Alireza Keshavarz, and Stefan Iglauer. H<sub>2</sub>- brine interfacial tension as a function of salinity, temperature, and pressure; implications for hydrogen geostorage. *Journal of Petroleum Science and Engineering*, 213:110441, 2022.
- [44] Bård J.A. Bjørkvik. What is the correct interfacial tension between methane and water at high-pressure/high-temperature conditions? *Fluid Phase Equilibria*, 572:113834, 2023. doi: <https://doi.org/10.1016/j.fluid.2023.113834>.
- [45] Y. T.Florence Chow, Geoffrey C. Maitland, and J. P.Martin Trusler. Interfacial tensions of the (CO<sub>2</sub> + N<sub>2</sub> + H<sub>2</sub>O) system at temperatures of (298 to 448) K and pressures up to 40 MPa. *Journal of Chemical Thermodynamics*, 93:392–403, 2016. ISSN 10963626. doi: 10.1016/j.jct.2015.08.006.
- [46] Catherine Spurin, Tom Bultreys, Branko Bijeljic, Martin J. Blunt, and Samuel Krevor. Mechanisms controlling fluid breakup and reconnection during two-phase flow in porous media. *Physical Review E*, 100(4):043115, 2019. doi: <https://link.aps.org/doi/10.1103/PhysRevE.100.043115>.
- [47] Bert Masschaele, Manuel Dierick, Denis Van Loo, Matthieu N. Boone,

- Loes Brabant, Elin Pauwels, Veerle Cnudde, and Luc Van Hoorebeke. HECTOR: A 240kV micro-CT setup optimized for research. *Journal of Physics: Conference Series*, 463:012012, 2013. doi: 10.1088/1742-6596/463/1/012012.
- [48] Hamed Aghaei, Ahmed Al-Yaseri, Ali Toorajipour, Behnam Shahsavani, Nurudeen Yekeen, and Katriona Edlmann. Host-rock and caprock wettability during hydrogen drainage: Implications of hydrogen subsurface storage. *Fuel*, 351:129048, 2023. doi: <https://doi.org/10.1016/j.fuel.2023.129048>.
- [49] Z. T. Karpyn, A. S. Grader, and P. M. Halleck. Visualization of fluid occupancy in a rough fracture using micro-tomography. *Journal of Colloid and Interface Science*, 307(1):181–187, 2007. doi: <https://doi.org/10.1016/j.jcis.2006.10.082>.
- [50] Yi Feng Chen, Shu Fang, Dong Sheng Wu, and Ran Hu. Visualizing and quantifying the crossover from capillary fingering to viscous fingering in a rough fracture. *Water Resources Research*, 53(9):7756–7772, 2017. doi: <https://doi.org/10.1002/2017WR021051>.
- [51] Shan Wang, Catherine Spurin, and Tom Bultreys. Pore-Scale Imaging of Multiphase Flow Fluctuations in Continuum-Scale Samples. *Water Resources Research*, 59(6):e2023WR034720, 2023. doi: <https://doi.org/10.1029/2023WR034720>.
- [52] Catherine Spurin, Maja Rücker, Marcel Moura, Tom Bultreys, Gaetano Garfi, Steffen Berg, Martin J. Blunt, and Samuel Krevor. Red Noise in

- Steady-State Multiphase Flow in Porous Media. *Water Resources Research*, 58(7):1–8, 2022. doi: <https://doi.org/10.1029/2022WR031947>.
- [53] Stephanie P. Bertels, David A. DiCarlo, and Martin J. Blunt. Measurement of aperture distribution, capillary pressure, relative permeability, and in situ saturation in a rock fracture using computed tomography scanning. *Water Resources Research*, 37(3):649–662, 2001. doi: <https://doi.org/10.1029/2000WR900316>.
- [54] Mohammad Piri and Zuleima T. Karpyn. Prediction of fluid occupancy in fractures using network modeling and x-ray microtomography. II: Results. *Physical Review E - Statistical, Nonlinear, and Soft Matter Physics*, 76(1):016316, 2007. doi: <https://doi.org/10.1103/PhysRevE.76.016316>.

# Supplementary Information for: "From underground natural gas to hydrogen storage in fractured reservoir rock : comparing relative permeabilities for hydrogen versus methane and nitrogen"

Sojwal Manoorkar<sup>a,b,\*</sup>, Gülce Kalyoncu Pakkaner<sup>a,b</sup>, Hamdi Omar<sup>a,b</sup>,  
Soetkin Barbaix<sup>a,b</sup>, Dominique Ceursters<sup>c</sup>, Maxime Lathinis<sup>c</sup>, Stefanie Van  
Offenwert<sup>c</sup>, Tom Bultreys<sup>a,b</sup>

<sup>a</sup>*Department of Geology, Ghent University, Ghent, Belgium*

<sup>b</sup>*Centre for X-ray Tomography (UGCT), Ghent University, Ghent, Belgium*

<sup>c</sup>*Fluxys, Belgium*

---

*Keywords:* Underground hydrogen storage, Relative permeability,  
Fractured rock, Hydrogen, Methane

---

## Contents

- Section S1: Fluid occupancy for fractional flows
- Section S2: Differential pressure
- Section S3: Sensitivity analysis: saturation
- Section S4: Nitrogen relative permeability comparison

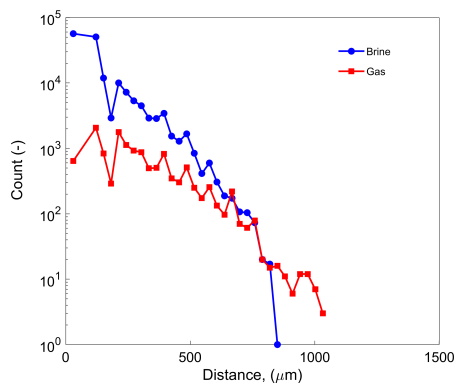
---

\*I am corresponding author

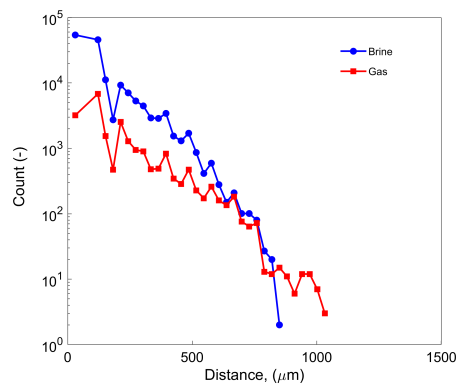
*Email address:* [sojwal.manoorkar@UGent.be](mailto:sojwal.manoorkar@UGent.be)/[sojwal.m@gmail.com](mailto:sojwal.m@gmail.com) (Sojwal  
Manoorkar )

## **1. S1: Fluid occupancy for fractional flows**

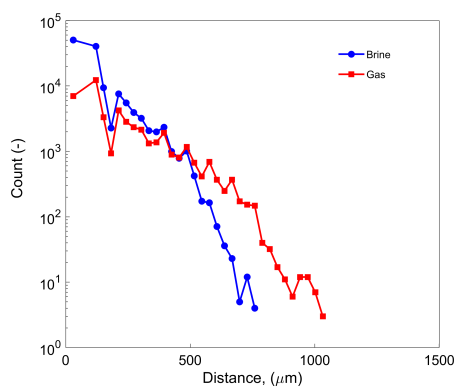
The skeleton derived from the distance map of the segmented dry fracture was utilized to generate these graphs. The segmented oil and brine phases were analyzed based on their proximity to the fracture walls. If the center of a fracture location was occupied by a specific fluid, that location was assigned to the corresponding fluid phase in the analysis. The fluid occupancy of brine and gas as a function of distance for varying fractional flows is presented in Figures 1, 2, and 3 for the hydrogen-brine, methane-brine, and nitrogen-brine experiments, respectively.



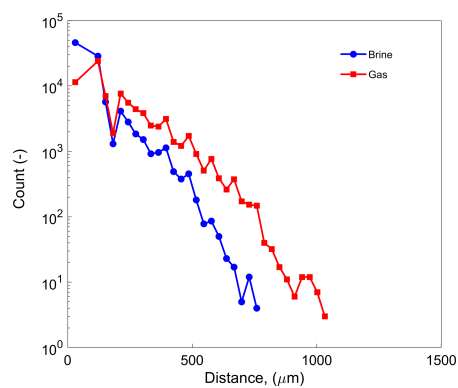
(a)



(b)

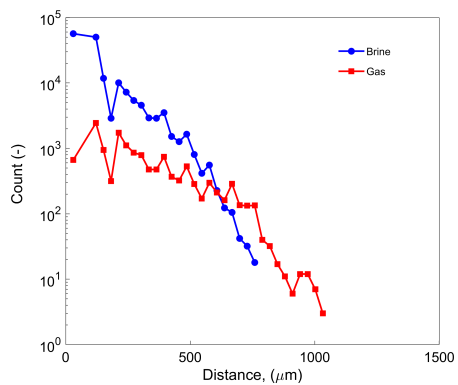


(c)

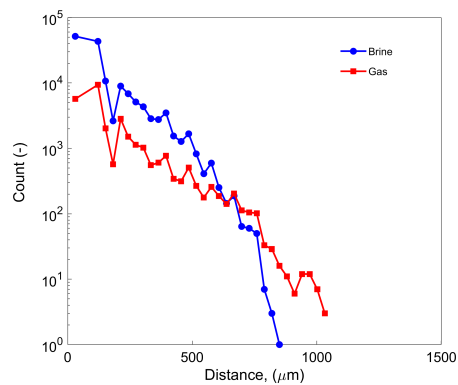


(d)

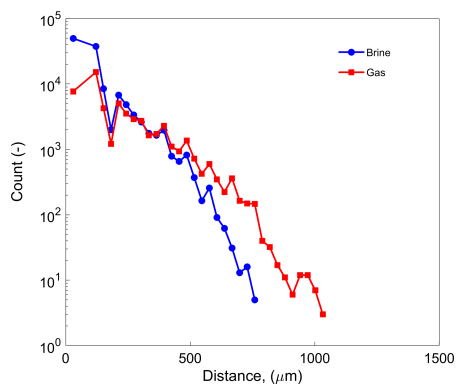
Figure 1: Fluid occupancy for various fractional flows for hydrogen - brine experiment (a)  $f_g = 0.1$  (b)  $f_g = 0.3$  (c)  $f_g = 0.8$  (d)  $f_g = 1$ .



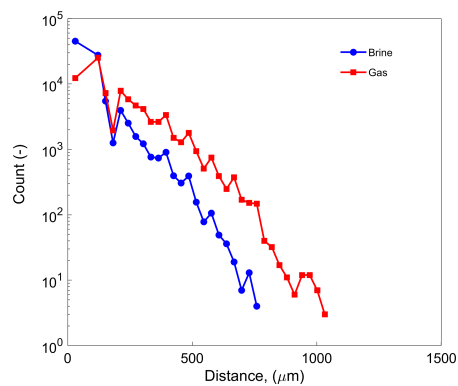
(a)



(b)



(c)



(d)

Figure 2: Fluid occupancy for various fractional flows for methane - brine experiment (a)  $f_g = 0.1$  (b)  $f_g = 0.3$  (c)  $f_g = 0.8$  (d)  $f_g = 1$ .

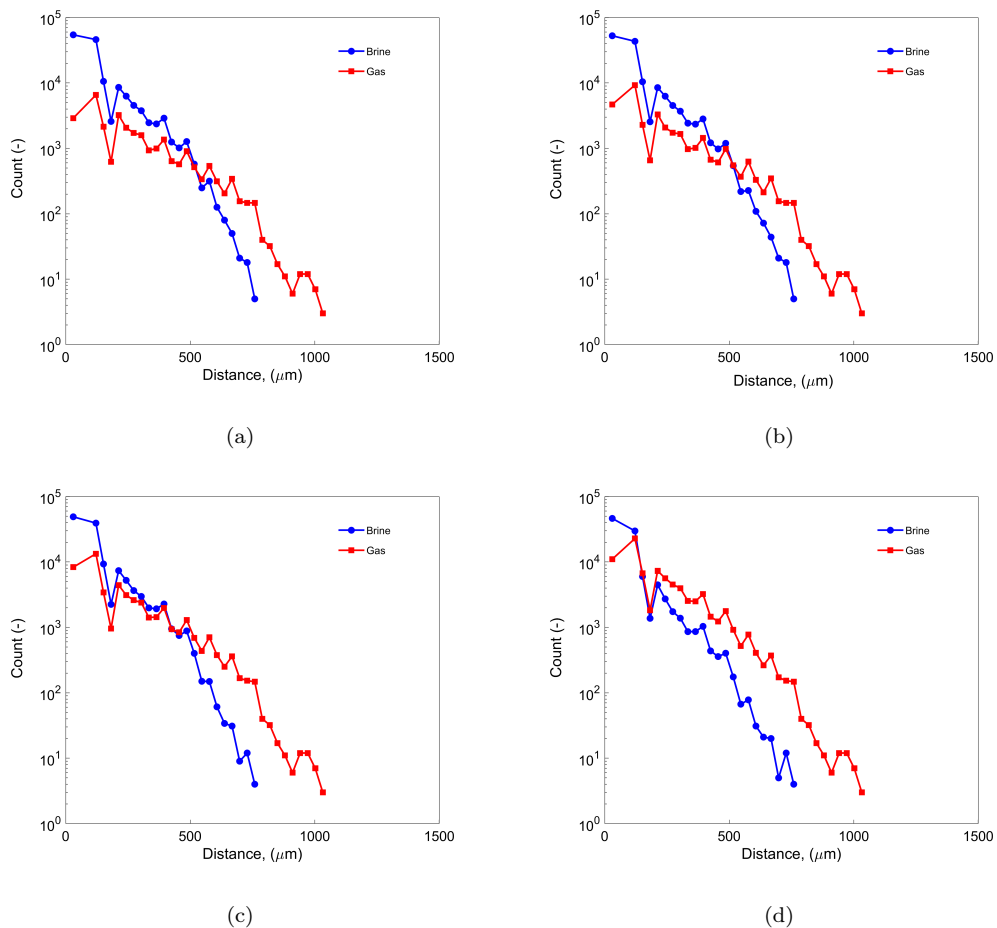


Figure 3: Fluid occupancy for various fractional flows for nitrogen - brine experiment (a)  $f_g = 0.1$  (b)  $f_g = 0.3$  (c)  $f_g = 0.8$  (d)  $f_g = 1$ .

## 2. S2: Differential pressure

The steady-state pressures for different fractional flows were measured using a differential pressure transducer (PD-33X) and are presented in Figures 4, 5a, and 5b for two runs each of the hydrogen, methane, and nitrogen experiments, respectively. Steady-state was achieved within 3 hours for the initial fractional flow, while subsequent fractional flows reached steady-state



within 2 hours. This equilibration time is significantly shorter compared to traditional core-flood experiments in porous media.

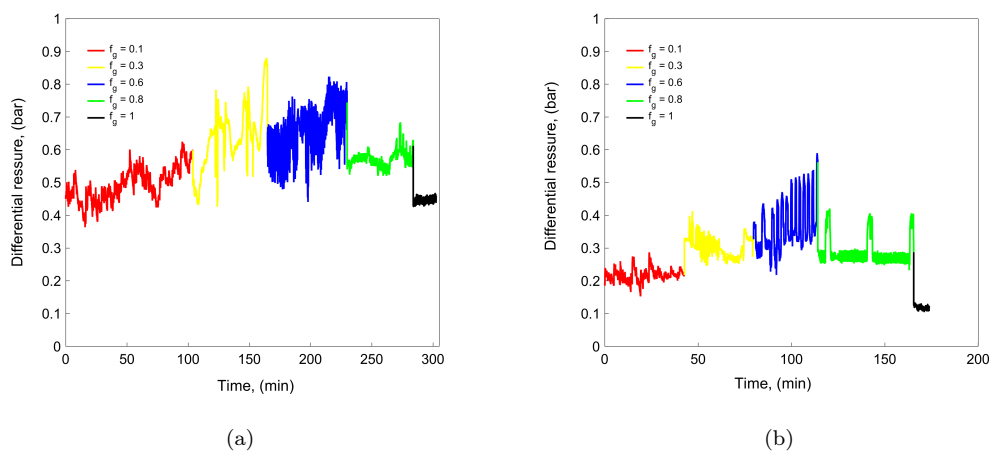


Figure 4: Steady-state differential pressure for varying gas fractional flow (a) Run 1 hydrogen-brine (b) Run 1 hydrogen-brine.

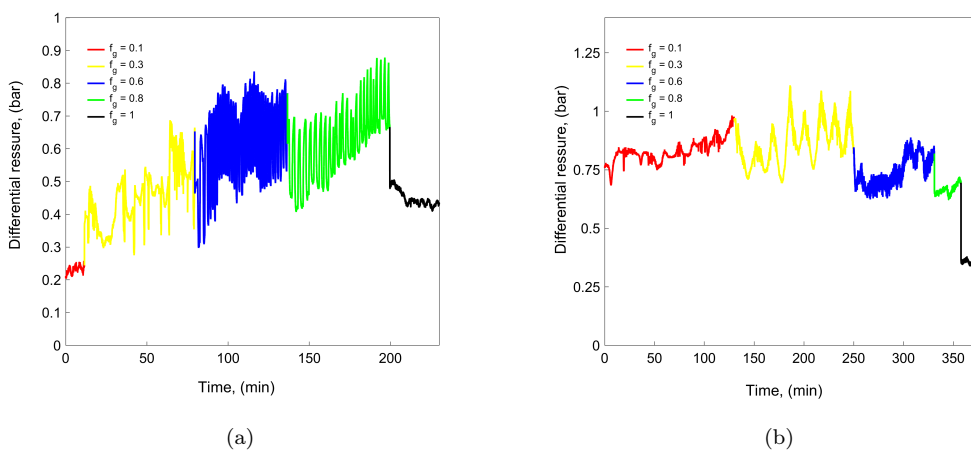


Figure 5: Steady-state differential pressure for varying gas fractional flow (a) methane - brine (b) nitrogen - brine.

### 3. S3: Sensitivity analysis : saturation

Figure 6 shows saturation profiles from two experimental runs at two different gas fractional flows. At a lower fractional flow ( $f_g = 0.1$ ), the saturation profiles exhibited significant variation, indicating greater intermittency in fluid distribution. With an increase in fractional flow to  $f_g = 1$ , the saturation profiles became more consistent, as illustrated in Figure 6b. The average saturation variation between the two runs was 6% for  $f_g = 0.1$  and 3% for  $f_g = 1$ . These observations suggest that the two-phase hydrogen-brine flow system is more susceptible to fluctuations at lower capillary numbers, where capillary forces strongly influence the flow. Despite these slight variations, the overall behavior remains consistent across both experimental runs, confirming that our workflow is robust and validating the results presented in this study.

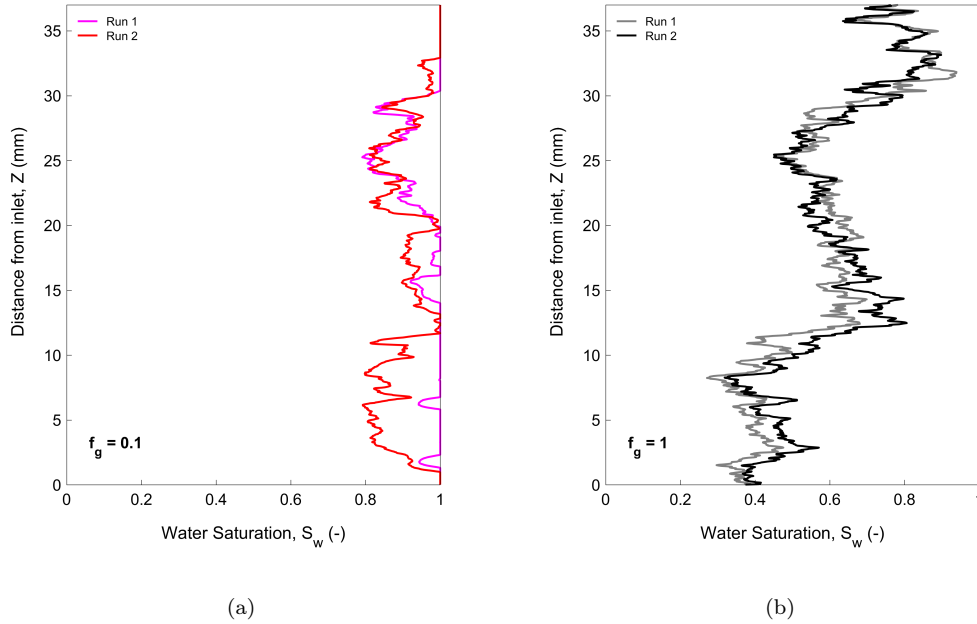


Figure 6: Saturation profile of brine for two experimental runs hydrogen-brine flow in fracture (a)  $f_g = 0.1$  (b)  $f_g = 1$ .

#### 4. S4: Nitrogen relative permeability : comparison to literature

The nitrogen-brine relative permeability is compared with experimental and numerical data from the literature for fractured media. The gas permeability for the nitrogen-brine system closely aligns with predictions by Gong et al. [1] for water-oil system, whereas the water permeability is lower than the model's prediction at the same water saturation.

Table 1: Fluid pairs used for relative permeability data from the literature.

Paper	Wetting phase	Non-wetting phase
Eliebid et al. [2]	1 wt% KCl	filtered Soltrol 170 mineral oil
Gong et al. [1]	water	oil
Watanabe et al. [3]	water	decane/nitrogen
Piri and Karpyn [4]	water	decane
Bertels et al. [5]	water	nitrogen
Persoff and Pruess [6]	water	air

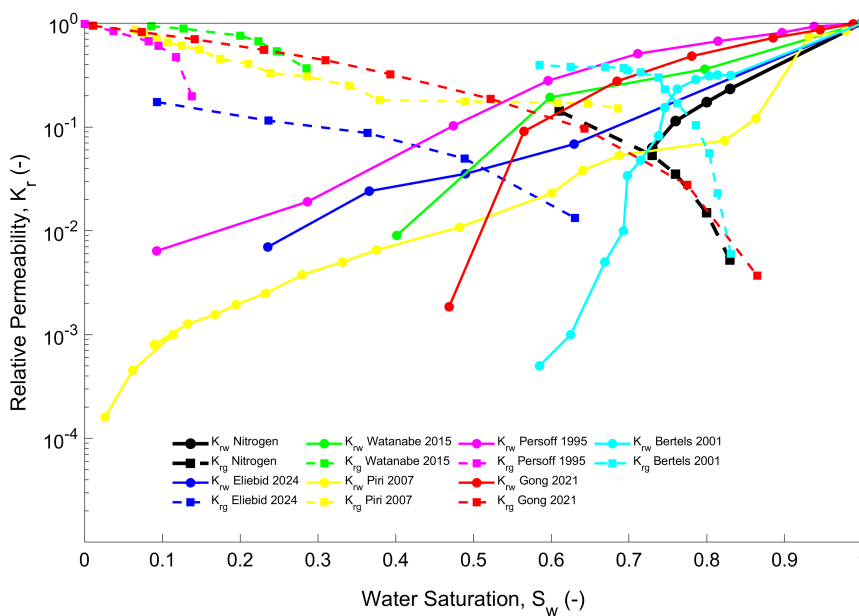


Figure 7: Comparison of nitrogen relative permeability from this study (black lines) with relative permeability models and experimental data for fractured media available in the literature.

Table 1 lists the different fluid pairs used in this study and those from the literature for comparison.

## References

- [1] Yanbin Gong, Mohammad Sedghi, and Mohammad Piri. Two-Phase Relative Permeability of Rough-Walled Fractures: A Dynamic Pore-Scale Modeling of the Effects of Aperture Geometry. *Water Resources Research*, 57(12), 2021. doi: <https://doi.org/10.1029/2021WR030104>.
- [2] Mohammed Eliebid, Abdelhalim Mohamed, Maziar Arshadi, Yanbin Gong, and Mohammad Piri. Relative permeability hysteresis and residual trapping in rough-walled fractures: An experimental investigation of the effects of flow rate and saturation history using the steady-state approach. *Advances in Water Resources*, 189:104729, 2024. doi: <https://doi.org/10.1016/j.advwatres.2024.104729>.
- [3] Noriaki Watanabe, Keisuke Sakurai, Takuya Ishibash, Yutaka Ohsaki, Tetsuya Tamagawa, Masahiko Yagi, and Noriyoshi Tsuchiya. New m-type relative permeability curves for two-phase flows through subsurface fractures. *JAWRA Journal of the American Water Resources Association*, 51(4):2807–2824, 2015. doi: <https://doi.org/10.1002/2014WR016515>.
- [4] Mohammad Piri and Zuleima T. Karpyn. Prediction of fluid occupancy in fractures using network modeling and x-ray microtomography. II: Results. *Physical Review E - Statistical, Nonlinear, and Soft Matter Physics*, 76(1):016316, 2007. doi: <https://doi.org/10.1103/PhysRevE.76.016316>.
- [5] Stephanie P. Bertels, David A. DiCarlo, and Martin J. Blunt. Measurement of aperture distribution, capillary pressure, relative permeability, and in situ saturation in a rock fracture using computed tomog-

raphy scanning. *Water Resources Research*, 37(3):649–662, 2001. doi: <https://doi.org/10.1029/2000WR900316>.

- [6] P. Persoff and K. Pruess. Two-Phase Flow Visualization and Relative Permeability Measurement in Natural Rough-Walled Rock Fractures. *Water Resources Research*, 31(5):1175–1186, 1995. doi: <https://doi.org/10.1029/95WR00171>.